ANTIMONIDE-BASED TYPE-II SUPERLATTICES FOR INFRARED DETECTION

BY

BENJAMIN A. KESLER

THESIS

Submitted in partial fulfillment of the requirements
for the degree of Master of Science in Electrical and Computer Engineering
in the Graduate College of the
University of Illinois at Urbana-Champaign, 2012

Urbana, Illinois

Adviser:

Professor Shun Lien Chuang

ABSTRACT

The vast array of applications for the detection of mid- to long-wave infrared radiation has spurred continuous interest in new and novel technologies to replace the current generation of state-of-the-art devices such as mercury cadmium telluride (MCT) detectors. One of the more promising alternatives is the type-II superlattice (T2SL), which was first proposed for infrared detection in 1978 and has been theoretically predicted to perform better than any MCT detector. Some advantages of the T2SL are its vastly improved electrical properties, material growth quality and cost, and the large number of degrees of freedom in tailoring the band structure to maximize performance at any given wavelength when compared to MCT detectors. However, the performance of T2SLs has been limited due to growth and fabrication problems, though the past decade has seen devices demonstrated with less than an order of magnitude difference in performance metrics when compared to commercially available MCT products, which is very promising for this material system.

This thesis presents only the second generation of T2SL devices grown via metal-organic chemical vapor deposition (MOCVD), and the first generation of devices grown on an InAs substrate by either molecular beam epitaxy (MBE) or MOCVD, an important fact for flip-chip bonding applications due to the lower absorption coefficient of InAs in the infrared when compared to the more common GaSb substrates. MOCVD is the preferred growth method in the industry, when available, due to its fast deposition rates with only a minimal sacrifice in growth precision when compared to MBE, so it is imperative that MOCVD T2SL devices quickly demonstrate performances similar to MBE grown T2SLs. A peak specific detectivity of 7.62×10^9 Jones at approximately 8 μm is reported, a 4.8 times increase from the value of 1.6 $\times 10^9$ Jones for the first MOCVD grown T2SL (which was grown on a GaSb substrate).

This thesis also addresses the reduction and elimination of surface leakage current, a dark current method that can be debilitating to device performance if not properly addressed. Promising results are achieved through the use of an ammonium sulfide soaking solution. In one instance, an almost one order of magnitude reduction of dark current densities is achieved using a neutralized ammonium sulfide solution, indicating that surface passivation is an important and necessary processing step. Future improvements, such as the usage of an encapsulating layer of polyimide or silicon nitride, are suggested in order to maintain the integrity of the ammonium sulfide passivation scheme and to physically protect the device itself.

To my family and friends, especially Nana, the best grandmother anyone could ever ask for

ACKNOWLEDGMENTS

I would like to begin by thanking the person who made my research at the University of Illinois possible: Professor Shun Lien Chuang. Thank you for giving me the opportunity to work in your optoelectronics laboratory and to grow and mature as a young scientist, both in the classroom and in the lab. Also, thank you for your personal invitation to come work for you, sent even before I had chosen to attend. It was your personal commitment that affirmed my desire to study at UIUC. Thank you for your guidance and help, both of which I have required numerous times. I know you and your family are going through a very tough time right now, but I know you'll continue to fight. Just know that I and the numerous others you have guided and taught are thinking about you and wishing you the very best. I would also like to thank everyone in the Chuang lab for all of the fun times and enlightening conversations we've had: Chien-Yao Lu, Akira Matsudaira, Adrian Ni, Michael Qiao, Daniel Zuo, Tommy O'Brien, and Meng Zhang. Without all your help, I certainly would have failed multiple times in my research endeavors, and I count myself lucky to have worked and still work with all of you.

A very sincere thank you goes out to all my friends from both Bedford and Emory (none of whom will ever read this thesis). I don't have enough space to name all of you individually but thanks for being there through the good and the bad. We've had some great times and will definitely have many more. Bingo.

Thank you to my sister, Sophia, my mom, Lydia, and all of my extended family for supporting and loving me for my 23 years on this Earth. I wouldn't be where I am today without your love, guidance, and sacrifice. Finally, thank you to my dad and role model, Morris, for teaching me what it means to be a true man of character and for instilling in me a love for science. Joey and Einstein, if you can read this I'll truly be impressed.

TABLE OF CONTENTS

CHAPTER 1

INTRODUCTION

1.1 Infrared Radiation and Applications

Infrared (IR) radiation, usually defined to be the range of wavelengths from 0.7 μm to 1000 μm, is an important region in the electromagnetic spectrum for a variety of sensing applications, particularly in the mid-wave (MWIR, 3–5 μm), long-wave (LWIR, 8–14 μm), and very-long-wave (VLWIR, 14–24 μm) infrared ranges. The wavelength range between the MWIR and LWIR (approximately 5–8 μm) contains a region of strong absorption due to water in the atmosphere, while other molecules contribute smaller absorption lines, such as carbon dioxide, which absorbs around 3.25 μm and 10.5 μm. According to Planck's law, all objects at thermal equilibrium radiate energy with a spectrum corresponding to the energy absorbed by the material, the wavelength of the radiation, and the temperature of the object itself, as seen in Fig. 1.1. In the case of a perfect blackbody, all incident energy is absorbed (zero reflection), and thus emitted, with the spectral radiance given by

$$B(\lambda, T) = \frac{2hc^2}{\lambda^5} \frac{1}{e^{\frac{hc}{\lambda k_B T}} - 1} \tag{1.1}$$

where T is the temperature, λ is the wavelength, c is the speed of light in a vacuum, h is Planck's constant, and k_B is the Boltzmann constant. The peak emission wavelength of the blackbody increases as the temperature of the blackbody decreases, while the emission intensity also decreases. In reality, a blackbody represents the upper limit of Planck's law and does not exist in nature, so the spectral radiance of a real object is

$$I(\lambda, T) = \varepsilon(\lambda) B(\lambda, T) \tag{1.2}$$

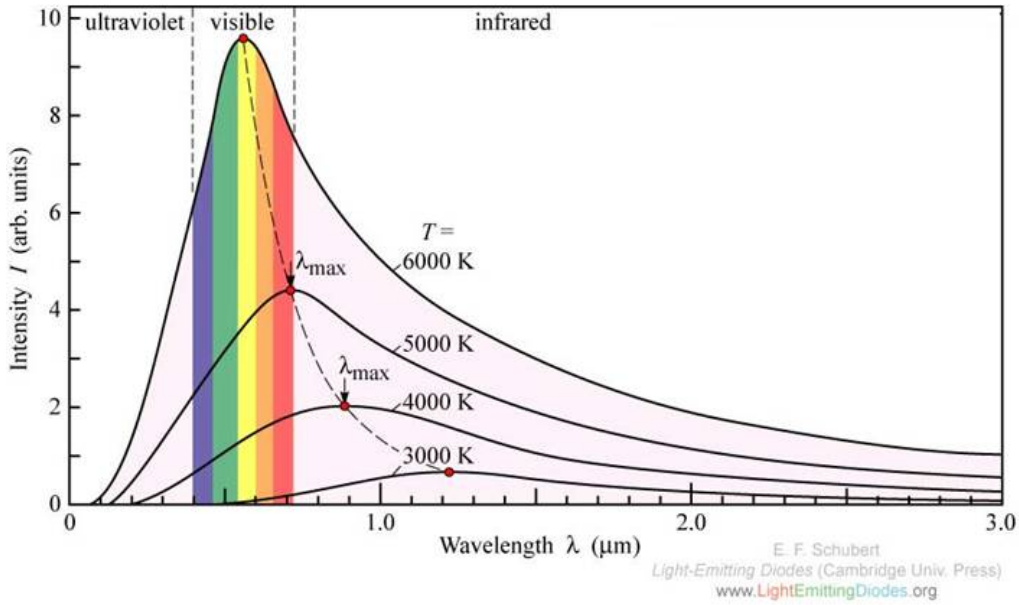

Figure 1.1: Wavelength dependent emission spectra for a blackbody at different temperatures. As the temperature of the blackbody drops, the wavelength of maximum emission increases while the intensity of the emission decreases. Adopted from Schubert [1].

where $\varepsilon(\lambda)$ is the emittance (or emissivity) of the object as a function of the wavelength and temperature, with lower and upper limits of 0 and 1, respectively. The more reflective an object is, the closer to 0 the emissivity becomes, while "blacker" or "darker" objects have emissivities that approach 1 at that wavelength and temperature. It is common and still accurate to assume some objects are true blackbodies, though they do not exist in reality. In some cases it is also accurate to assume objects are greybodies, which are objects that have a constant emissivity of less than one over all wavelengths, meaning some incident radiation is reflected, with an emission curve that still follows the same trend as a perfect blackbody.

As an example, the peak wavelength of emission of the Sun, which has a surface temperature of approximately 5500 K, is in the visible regime at about 660 nm. However, most objects on Earth, including humans, have temperatures that fall somewhere around 300 K, corresponding to a peak emission wavelength of 10 μm. As such, the MWIR to VLWIR portions of the spectrum are of great interest for military and industrial applications. Some applications that utilize the blackbody nature of objects are thermal imaging, which collect the radiation emitted by living and inanimate objects

to create a picture of the world even in darkness, medical diagnostics, which can image cancerous growths or other deformities inside the human body in a non-invasive manner, and heat seeking missile technology, which operates by tracking the exhaust plumes of planes or other missiles. Other applications include gas sensing and pollution analysis, which utilize the fact that many molecules and other organic compounds have distinct and identifiable absorption lines in the infrared regime by collecting light from a blackbody source in a gas filled chamber and observing where these lines are located, and free space communication.

1.2 Infrared Detection

Some of the current, commercially available infrared detectors for the MWIR to VLWIR are the bulk, II-VI semiconductor mercury cadmium telluride (MCT) detectors and the quantum well infrared photodetector (QWIP). QWIPs are devices that contain one or more quantum wells and use intersubband transitions to generate electrons in the wavelength range corresponding to the bandgap of the optical transition, which can be tailored to specific wavelengths by changing the well width. They are typically grown on a GaAs substrate and use AlGaAs as the barrier and n-doped GaAs as the well material such that the Fermi level is between the ground state and first excited energy levels of the quantum well so as to provide the free electrons needed in the ground state for photon absorption transitions. There are three main types of transitions that can occur in QWIPs, shown in Fig. 1.2, depending on their design: bound-to-bound, where the wavefunctions of both energy states are confined within the well, bound-to-quasibound, where the wavefunction of the upper energy state is aligned with the top of the well, and bound-to-continuum, where the upper energy level is located in a miniband of states that spans the entire device. One major problem with QWIPs is that the optical matrix element for TE (normal incident) radiation is zero due to the optical selection rule, meaning light must be incident on the detector either from the side or at an angle for transitions from the ground miniband to the first excited state miniband to occur. One solution for this situation that is typically employed is to use a grating or pattern on the top of the device that is designed to angle any normal incident light. One other

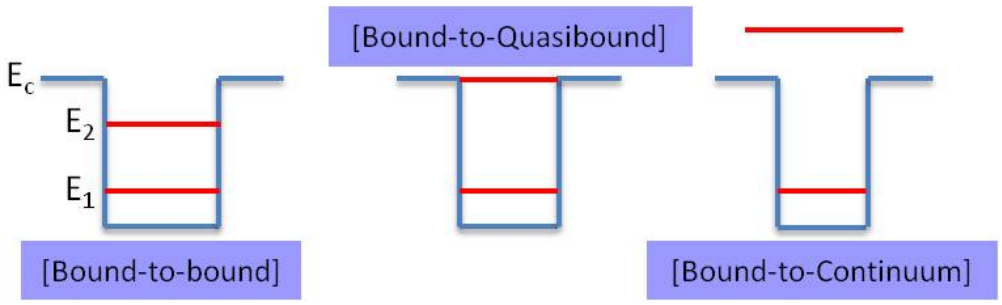

Figure 1.2: Three intersubband transitions that can occur in an n-doped quantum well infrared photodetector (QWIP), depending on the design of the wells themselves. QWIPs suffer from the inability to absorb normal (TE) incident light, a small spectral range, and low efficiencies due to the nature of the transition that occurs with the absorption of a photon.

feature of QWIPs that could be considered a drawback for their use in certain situations is their small spectral range. Since the transitions in a QWIP are intersubband, the effective masses of the particles involved, electrons in this case, are the same, meaning the absorption spectrum of the QWIP can be written as a Lorentzian of a certain linewidth [2]. This is unlike situations, such as those involving electrons and holes, where the effective masses are different and the absorption spectrum takes a much more complicated form, yet has a larger spectral range that can span many microns.

MCT ($Hg_{1-x}Cd_xTe$) infrared detectors are bulk photodiodes that employ optical transitions between the valence and conduction bands of the material to detect infrared radiation. Some advantages of the MCT detectors are a wide spectral response range and tunable bandgap, obtainable by changing the mercury mole fraction, from 3 to 30 μm. There are a few problems associated with using MCT, particularly in the LWIR regime. First, the bandgap of an MCT detector is very sensitive to the mercury (Hg) mole fraction and, as it turns out, the composition control needed for a detector with a cutoff wavelength (λ_{cutoff}) of greater than 14 μm is "less than 0.2% variation in x" [3]. Another concern is the cost of the device wafers themselves: bulk MCT wafers are typically grown on cadmium zinc telluride (CdZnTe) substrates, which are expensive even at the 3 inch size and hard to grow for larger sizes [4]. Also, the larger MCT wafers are nonuniform over their entirety when it comes to material makeup meaning that the bandgap of devices fabricated using the entire wafer can change dramatically due to the aforementioned sensitivity of the bandgap on Hg mole fraction [5, 6]. Finally, large cooling

units are still needed, as these detectors operate at cryogenic temperatures.

Despite these drawbacks, MCT detectors are the most commonly used commercial material system for MWIR to VLWIR detection, consistently exhibiting the best performance. However, the past few decades have seen the rising of a fairly new material system known as the type-II superlattice (T2SL), the performance of which has been theoretically predicted to be better than that of MCT detectors, even at higher temperatures. Also, T2SL wafers are grown using the mature growth processes of III-V materials, which can achieve consistent uniformity even over larger wafer sizes.

1.3 The Type-II Superlattice (T2SL)

Type-II superlattices (T2SL) began to emerge over the past few decades as a viable alternative to MCT detectors. The superlattice structure was first proposed in 1970 by Esaki and Tsu [7], but it was not until 1978 when the InAs/GaSb T2SL structure was linked to possible infrared detection applications [8]. A T2SL is a series of thin, alternating layers of semiconductor alloys, typically InAs, GaSb, or AlSb, with a total period of less than 10 nm and a staggered energy band lineup. In the case of InAs/GaSb, the bottom of the InAs conduction band is lower than the top of the GaSb valance band by about 150 meV. This unique band structure serves to confine electrons and holes in spatially different positions, with the electrons confined in the InAs layers and the holes in the GaSb layers, a rough schematic of which is shown in Fig. 1.3. Each layer can be considered as a single quantum well, so the coupling and splitting between the electron or hole states in the different wells creates conduction and valence minibands. The difference between the bottom of the first conduction miniband and the top of the first heavy hole miniband is the effective bandgap of the T2SL and determines the cutoff wavelength – the longest wavelength which will be absorbed and excite carriers – of the detector. The important thing to note is that the effective bandgap is inherently smaller than the bandgap of InAs (0.354 eV) or GaSb (0.726 eV) due to the staggered band alignment and spatial separation of the electrons and holes, meaning cutoff wavelengths from 3 to 30 μm can be realized simply by changing the layer widths. However, this feature is not without its drawbacks: to reach longer cutoff wavelengths the layer

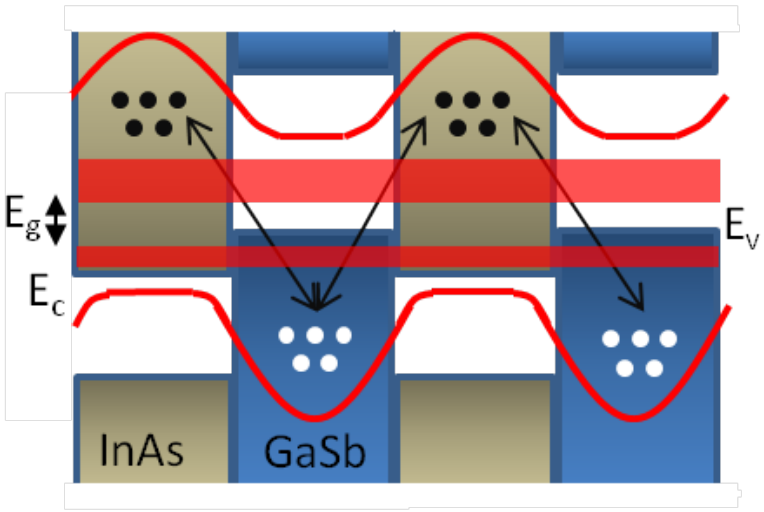

Figure 1.3: Type-II alignment band structure for an InAs/GaSb superlattice. The electrons (black circles) and holes (white circles) are spatially separated and located in the InAs and GaSb layers, respectively. Coupling and splitting between the electron and hole states in the different wells creates conduction and valence minibands, with the difference between the bottom of the first conduction band and the top of the first heavy-hole valence band being the effective bandgap of the T2SL.

thicknesses need to be increased, resulting in a decrease in the wavefunction overlap and optical matrix element between the electrons and holes.

MCT and T2SL detectors are predicted to have roughly the same absorption coefficient near the band edge, a result that spurred great interest in T2SLs as a commercially viable detector [9]. One of the main reasons to explain the comparable absorption coefficients comes from the density of states. As it turns out, the electron effective mass in the both the growth and transverse directions (though the band diagram is very anisotropic) for a T2SL, $m_e^*/m_0 \simeq 0.03$–0.04, is significantly larger than in MCT, where $m_e^*/m_0 \simeq 0.008$–0.01, leading to a larger density of states for the T2SL and compensating for its smaller optical matrix element [9]. The larger electron effective mass also serves to greatly decrease tunneling dark currents in T2SLs, the limiting mechanism in VLWIR MCT detectors, while still maintaining good mobilities, diffusivities, and diffusion lengths [10].

One of the other main advantages of T2SLs over MCT detectors has to do with the material growth precision involved, particularly for longer cutoff wavelength structures. As mentioned previously, the bandgap of MCT detectors is tailored by varying the Hg mole fraction, while it is varied in

T2SLs by increasing or decreasing the width of the semiconductor layers (as well as mole fractions if using a ternary alloy). As it turns out, the bandgap of $Hg_{1-x}Cd_xTe$ can change from 19 μm to 17 μm for a Δx of only 0.004, and this effect is only exacerbated as the bandgap shrinks. The same change in cutoff wavelength requires $\Delta x = 0.03$ for the InAs/$In_xGa_{1-x}Sb$ ternary T2SL structure (which will be discussed in more detail later), nearly an order of magnitude increase [11]. As for layer thicknesses, a monolayer change of InAs for a detector designed for a cutoff wavelength of $\lambda_{co} = 20$ μm will change the cutoff wavelength by approximately 3 μm [3]. Fortunately, T2SLs are typically grown by molecular beam epitaxy (MBE), a very precise growth method that can achieve better than half monolayer fluctuations in layer widths [3], so changes in cutoff wavelengths due to layer width errors are minimized even at very low bandgap energies.

It was not until nearly a decade after the proposition of InAs/GaSb T2SLs as an infrared detector material system that the next major breakthrough in T2SL theory occurred. In 1987, Smith and Mailhoit added In to the GaSb binary layers, forming the ternary $In_xGa_{1-x}Sb$ alloy, and calculated the effect on the effective bandgap of the T2SL and other properties such as the absorption coefficient [9]. One immediate difference between InAs/GaSb and InAs/$In_xGa_{1-x}Sb$ grown on a GaSb substrate is the additional strain component that alters the energy band structure of the ternary alloy.

Figure 1.4, taken from [9], shows the bulk unstrained energy positions for bulk InAs, GaSb, and InSb (a), and the strained energy positions for bulk InAs and $In_{0.4}Ga_{0.6}Sb$ grown on a GaSb substrate (b). As is well known, the InAs undergoes tensile straining due to the fact that it has a smaller lattice constant than GaSb, which pushes the conduction band (CB) down and splits the light hole (LH) band up and heavy hole (HH) band down from the valence band (VB). The $In_{0.4}Ga_{0.6}Sb$ layer has a larger lattice constant than GaSb so it undergoes compressive strain, which pushes the CB up and splits the HH and LH up and down, respectively, from the VB. Since optical transitions in T2SLs near the band edge are generally between the first CB and the first HH minibands, the splitting of the HH energy band upward is equivalent to splitting the entire HH1 miniband upward by the same amount, reducing the effective bandgap. Thus, in order to achieve the same cutoff wavelengths, thinner $In_xGa_{1-x}Sb$ layers can be used when they replace GaSb, increasing the hole wavefunction leakage, the electron-hole wavefunction overlap, and

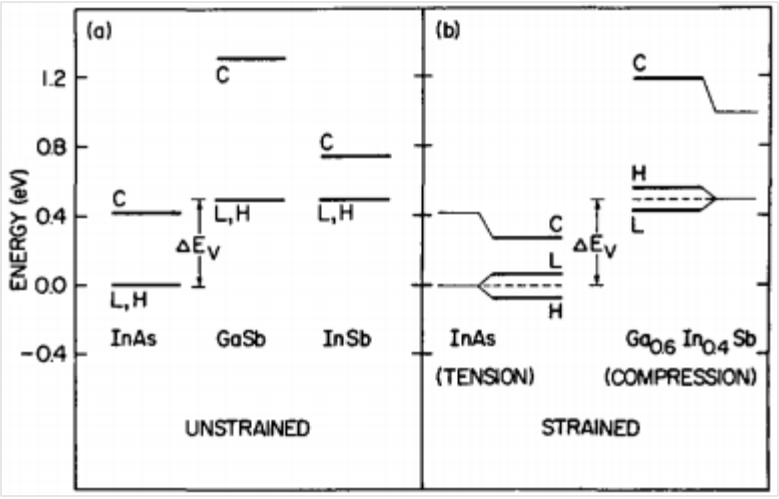

Figure 1.4: (a) Unstrained energy band levels for bulk InAs, GaSb, and InSb. (b) Strained bulk energy band levels for bulk InAs and $In_{0.4}Ga_{0.6}Sb$ grown on a GaSb substrate. The tensile strain on the InAs layers shifts the conduction band downward while the compressive strain on the $In_{0.4}Ga_{0.6}Sb$ layers splits the heavy-hole valence band upward, meaning thinner layers can be used to achieve the same cutoff wavelengths as an InAs/GaSb structure. From [9].

the absorption coefficient.

Another benefit of the increased splitting is the reduction in the nonradiative Auger recombination, specifically the inter-valence-band hole-hole Auger transitions, which are one of the limiting dark current mechanisms in MCT detectors for cutoff wavelengths greater than 8 μm. Since quantum wells that are grown on bulk substrates already have inherent HH and LH band splitting, the Auger reduction due to the strain splitting of the valence band serves to reduce the Auger recombination rates even further and increase the Auger lifetimes by, in some cases, nearly three orders of magnitude for T2SLs when compared with MCT detectors [12]. However, it is important to note that the total amount of splitting between either the first heavy-hole and first light-hole (HH1/LH1), or first heavy-hole and second heavy-hole (HH1/HH2), bands needs to be larger than the effective bandgap of the T2SL to reduce Auger recombination near the Brillouin zone center. Also, the Auger reduction is only noticeable at low (cryogenic) temperatures, and is still one of the dominating dark current mechanisms in both InAs/GaSb and InAs/$In_xGa_{1-x}Sb$ T2SLs at room temperature [13].

The most common T2SL photodiode structure is a *p-i-n* diode, where a

large, unintentionally doped absorber region is sandwiched in between the heavily doped p and n contacts of the device. There are many considerations when growing even this "simple" T2SL structure, the first of which is strain compensation through the use of interfacial (IF) layers. Considering an InAs/GaSb T2SL, if there is no intentional strain compensation (so the IF layers are considered to be random), the IF layers will either be GaAs-like or InSb-like binary, ternary, or even quaternary alloys. However, the choice of IF layers is actually a critical step in the growth of the T2SL due to their influence on interface roughness (defects), effective bandgap, absorption coefficient, and strain compensation. For example, the use of InSb-like interfacial layers results in a slight redshift of the cutoff wavelength of InAs/GaSb layers because of the compressive strain due to the large lattice constant, while using GaAs-like IF layers results in a slight blueshift of the cutoff wavelength [14]. Other considerations for the IF layers used are the roughness and abruptness of the interface itself, which needs to be reduced and increased, respectively. It has been shown that InSb-like IF layers are not only smoother than GaAs-like layers, but they are also more abrupt (whereas no control of IF layers results in the most diffuse and least desirable interfaces) [3]. In the end, the choice of IF layers is most important for strain balancing the several-micron-thick T2SLs, as the lattice mismatch of the SL compared to the substrate needs to be kept below $\pm 5 \times 10^{-3}$ [3].

The doping in the absorber region of a T2SL, whose residual background carrier concentration must be made as small as possible, is another important factor. As it turns out, it is more beneficial to grow T2SLs on a p-type GaSb substrate in the n-on-p configuration, where the absorber region is lightly p-doped, forming a p^+-p-n^+ diode. The reason for this becomes apparent when looking at the energy band structures (not shown) of typical InAs/GaSb or InAs/InGaSb superlattices. In the growth direction, the effective mass of holes is much heavier than that of the electrons, making them harder to collect [9]. Thus, it is desirable to have electrons as the minority carriers in the absorber region, hence the light p-doping, which results in not only better vertical transport properties but a further reduction in Auger recombination rates with only a minimal decrease in the wavelength dependent absorption coefficient due to the introduction of extra holes in the VB and no change in cutoff wavelength [14].

1.4 Thesis Overview

This work focuses on the fabrication and characterization T2SLs grown by both metal-organic chemical vapor deposition (MOCVD) and molecular beam epitaxy (MBE). MOCVD technology has only recently been applied to T2SL growth, fabrication, and characterization on GaSb substrates in the past few years [15, 16], and the samples used in this work represent the second generation of MOCVD T2SLs, but the first ever on an InAs substrate [17].

Chapter 1 focuses on the relevant background information regarding infrared radiation and the applications involving its detection. It also describes two of the most popular commercially available material systems used for infrared detection: mercury cadmium telluride (MCT) detectors and quantum well infrared photodetectors (QWIPs). Finally, a description of T2SLs is provided that includes explanations about the bandstructure of the system and certain properties that make T2SLs theoretically predicted to perform better than their MCT counterparts.

Chapter 2 introduces important figures of merit and the state-of-the-art of T2SLs, as well as explanations about the many novel structures that are being used to further improve the performance of the material system. Also mentioned are the dark current mechanisms that are prevalent during T2SL operation and are currently limiting the effectiveness of fabricated devices.

Chapter 3 describes the fabrication methods used in the creation of the T2SL photodiodes and the subsequent characterization methods used. Fabrication was done using either wet or dry etching mechanisms designed to produce the mesas used for photodetection, while the characterization methods include current-voltage measurements, response measurements using a Fourier transform infrared spectrometer (FTIR), and a calibration measurement using a source that is approximated as a perfect blackbody.

Chapter 4 presents background and data on a new T2SL system grown on an InAs substrate via MOCVD. The InAs substrate is the first of its kind, and its advantages over traditional GaSb substrates are discussed both theoretically and experimentally. Data for the first generation of InAs/GaSb T2SLs grown on this InAs substrate via MOCVD is presented, and a 4.8 times increase in performance over the first generation of MOCVD grown T2SLs, grown on a GaSb substrate, is recognized.

Chapter 5 discusses the effect of light p-doping on the electrical properties

of MBE grown InAs/GaSb T2SLs purchased from IQE. The light p-doping in the absorber region results in the minority carriers being the electrons, which is beneficial because of their superior electrical properties when compared to the much heavier holes in the superlattice.

Chapter 6 touches on the importance of passivation for the device performance of T2SLs. Surface leakage current has an extremely important and debilitating effect on the electrical characteristics of T2SLs, meaning effective, efficient, and long-lasting passivation methods must be developed. A brief synopsis of different passivation methods is included, followed by the passivation of MOCVD grown T2SLs on an InAs substrate by ammonium sulfide solutions.

Chapter 7 summarizes this work and outlines future work that will be, and should be, conducted in order to improve the performance of not only the state-of-the-art MBE grown T2SL samples, but the MOCVD samples as well.

CHAPTER 2

T2SL STATE-OF-THE-ART

2.1 Figures of Merit

When talking about the performance of T2SL infrared photodetectors, and infrared photodetectors in general, there are several well-established figures of merit that are most commonly used [2, 18, 19]. In fact, some of these figures of merit allow for comparison between infrared detectors of the same type (such as photovoltaic detectors) but of completely different areas or material systems (such as MCT vs. T2SL vs. QWIP). This section describes these figures of merit, which will be used throughout the text.

2.1.1 Cutoff Wavelength

The most basic figure of merit used when describing infrared detectors is the cutoff wavelength, which is defined as the maximum wavelength of a photon that can be absorbed by the detector to create an electron-hole pair (or, in the case of QWIPs, the creation of a higher energy electron in the conduction band). The cutoff wavelength can be defined in terms of the bandgap of the detector in question, and is calculated as

$$\lambda_{cutoff} = \frac{hc}{E_g} \simeq \frac{1.24}{E_g} \tag{2.1}$$

where λ_{cutoff} is the cutoff wavelength in μm, h is the Planck constant in eV/s, c is the speed of light μm/s, and E_g is the bandgap of the detector in eV.

In bulk materials such as MCT, the cutoff energy is simply the bandgap of the material itself and can be easily calculated using the mole fractions of the constituent materials and the well-known bowing parameters, and in

QWIPs the bandgap is the energy difference between the first and second conduction band excited states (such as those shown in Figure 1.2. However, in T2SLs the bandgap is the difference between the bottom of the first conduction miniband and the top of the first heavy hole miniband, which can be determined from the band structure at the center of the Brillouin zone. The band structure is not easily calculated, requiring tools such as the 8-band $k \cdot p$ method demonstrated in [14].

2.1.2 Differential Resistance at Zero Bias Area Product (R_0A)

Noise behavior in a photovoltaic detector is quantified through a metric known as the differential resistance at zero bias area product, which is more commonly labeled as the dynamic resistance at zero bias, or R_0A. The unit of the R_0A product is typically given in Ωcm^2. The R_0A product can be calculated from the measured current-voltage (IV) curve by

$$\frac{1}{R_0A} = \left[\frac{dJ}{dV}\right]_{V=0} = \left[\frac{1}{A}\frac{dI}{dV}\right]_{V=0} = \frac{eI_0}{k_BT} \tag{2.2}$$

where J is the current density, V is the bias voltage, A is the physical area of the photodiode (*not* the optical area, which can be significantly smaller depending on the top contact configuration), k_B is the Boltzmann constant, T is the temperature, and I_0 is the reverse current of the ideal photodiode.

In theory, the value of the R_0A product should remain constant for all devices of the same material system regardless of the perimeter-to-area ratio, P/A, or etching method used to etch the device. This constant value is simply the bulk dynamic resistance at zero bias, or R_0A_{bulk}, determined from an ideal T2SL diode curve. However, surface defects such as native oxides (In_2O_3 in InAs or InSb) formed from the exposure of the sidewall to the ambient atmosphere [20], dangling bonds formed from the abrupt termination of the periodicity of the atoms at the sidewall, and etching or mask byproducts resulting from fabrication can severely impact the performance of the device. Charged defects cause band bending and Fermi-level pinning at the surface [21, 22], which results in inversion layers and subsequent channels for dark current, while neutral defects increase trap-assisted tunneling [23]. Thus, the

R_0A product can be written as

$$\frac{1}{R_0A} = \frac{1}{(R_0A)_{bulk}} + \frac{1}{\rho_{surface}}\frac{P}{A} \tag{2.3}$$

where P is the perimeter of the device mesa in cm, A is the total area of the device mesa in cm^2, R_0A_{bulk} is the previously mentioned bulk dynamic resistance at zero bias in Ωcm^2, and $\rho_{surface}$ is the surface resistivity of the device in Ωcm. For a device with infinite surface resistivity, the plot of R_0A^{-1} vs. P/A would yield a straight line. Surface resistivity can be reduced or eliminated through the use of surface passivation methods, which will be discussed further in Chapter 6.

2.1.3 Responsivity

The responsivity of a detector is a measure of the electrical output signal of the device relative to the input radiation power and is given by

$$R(\lambda) = \frac{I_s(\lambda)}{\Phi_e} \tag{2.4}$$

where $I_s(\lambda)$ is the measured output photocurrent of the device in amperes and Φ_e is the spectral radiant incident power on the device in watts, giving responsivity the unit of A/W. The technique used for the calculation of the responsivity of T2SL devices is discussed in Chapter 3.

2.1.4 Quantum Efficiency (QE)

The quantum efficiency of a device can be defined in two ways: internal and external. External quantum efficiency is a measure of the number of electron-hole pairs generated per incident photon and can be written in terms of the responsivity as

$$\eta(\lambda)_{external} = R(\lambda)\frac{hc}{\lambda q} \tag{2.5}$$

where $R(\lambda)$ is the responsivity in A/W, h is the Planck constant, c is the speed of light, λ is the wavelength, and q is the elementary charge constant, making the quantum efficiency a unitless value. This definition accounts for the loss of any photons due to reflection off the front surface of the detector

and the loss of any electrons due to recombinations. The internal quantum efficiency considers photon loss due to reflection and can be written in terms of the external quantum efficiency and reflection coefficient as

$$\eta(\lambda)_{internal} = \eta(\lambda)_{external}\frac{1}{1-R} \tag{2.6}$$

where R is the power reflectivity of the front surface. The internal quantum efficiency can, in theory, be equal to 1 while the external quantum efficiency is limited to a value of $1 - R$.

2.1.5 Specific Detectivity

Simply put, the specific detectivity is a figure of merit that permits comparisons of detectors of different area, as long as they are of the same type (such as photovoltaic). It is a measure of the sensitivity of the detector and is defined as

$$D^*_\lambda = \frac{\sqrt{A\Delta f}}{NEP} = R(\lambda)\sqrt{\frac{A\Delta f}{\langle i_n^2\rangle}} \tag{2.7}$$

where NEP is the noise equivalent power (the input power that produces a signal to noise ratio of exactly 1) in watts, A is the area of the device, Δf is the electrical noise bandwidth, $R(\lambda)$ is the responsivity, and $\langle i_n^2\rangle$ is the noise current. In the case of a photovoltaic detector such as a T2SL (which is commonly operated at zero bias), the detector is thermally, or Johnson noise, limited [19] and the specific detectivity can be written in terms of the R_0A product as

$$D^*_\lambda = R(\lambda)\sqrt{\frac{R_0A}{4k_BT}} \tag{2.8}$$

which has units of cm·Hz$^{1/2}$/W, or Jones.

2.2 Dark Current Mechanisms

In T2SLs there are several dark current mechanisms that will negatively affect device performance by limiting the excess minority carrier lifetime and reducing the differential resistance at zero bias area product (R_0A), a figure of merit that quantifies the noise of a photodiode. As discussed previously,

Auger recombination is heavily suppressed in T2SLs, which should result in Auger limited lifetimes of almost $\tau_e = 700$ ns for a device with a cutoff wavelength of approximately 140 meV at T = 77 K [24]. However, numerous experimental results reported over the past few decades have confirmed that T2SLs are limited by different dark current mechanisms over different temperature ranges and the excess minority carrier lifetimes are limited to, at most, tens of nanoseconds due to generation-recombination processes at liquid nitrogen temperatures. However, very encouraging minority carrier lifetimes were published recently for the new T2SL layer structure system of InAs/InAsSb. Though the total period was extremely large (24.5 nm), the minority carrier lifetimes reported were in excess of 412 ns at 77 K, a promising result for this new T2SL, and attributed to the removal of Ga from the layer structure, which led to a reduction of non-radiative generation-recombination centers [25].

Overall, T2SLs are limited by trap assisted tunneling currents at temperatures below 50 K, generation-recombination (specifically Shockley-Read-Hall [SRH]) currents from T = 50 K to T $\simeq$ 85 K, and diffusion currents above 85 K. Figure 2.1 plots the measured and simulated R_0A values as a function of operating temperature for an 11 μm cutoff wavelength InAs/InGaSb T2SL, with the limiting components easily identifiable [26].

According to [26], which offers the theoretical analysis presented below, there are four main dark current components that contribute to the noise in T2SL detectors and limit the R_0A product: the diffusion dark current, generation-recombination (GR) dark current, Zener tunneling dark current, and trap-assisted tunneling dark current. The following equations have been derived assuming a uniform electric field in a neutral depletion region (and, therefore, a triangular potential barrier).

1. The diffusion current, or J_{diff}, is a result of thermally excited carriers being swept along the gradient in carrier concentration between the p and n regions of the diode and can be written as

$$J_{diff} = n_i^2 \sqrt{e k_B T} \left(\frac{1}{N_A} \sqrt{\frac{\mu_e}{\tau_e}} + \frac{1}{N_D} \sqrt{\frac{\mu_h}{\tau_h}} \right) \left(e^{eV/k_B T} - 1 \right) \qquad (2.9)$$

   where μ_e and τ_e are the electron mobility and lifetime, respectively, μ_h and τ_h are the hole mobility and lifetime, respectively, q is the

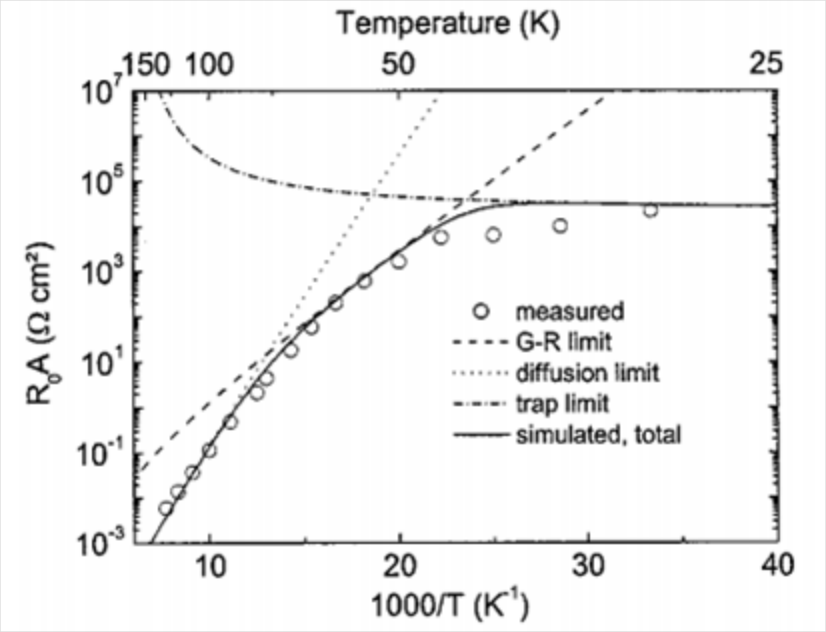

Figure 2.1: Graph of measured and simulated total and individual dark current component limited R_0A vs. T and 1000/T for an InAs/InGaSb T2SL with a cutoff wavelength of 11 μm. From [26].

elementary charge constant, k_B is the Boltzmann constant, T is the temperature, n_i is the intrinsic carrier concentration, and N_A and N_D are the p- and n-type doping concentrations.

2. Generation-recombination (G-R) dark current occurs in the depletion region and can be written as

$$J_{GR} = \frac{en_i d(V)}{\tau_{GR}} \frac{sinh(-eV/2k_BT)}{e(V_{bi}-V)/ek_BT} f(b) \tag{2.10}$$

$$f(b) = \int_0^\infty \frac{du}{u^2+2bu+1},\ b = exp\left(\frac{-eV}{2k_BT}\right)$$

where V_{bi} is the built-in potential of the diode, τ_{GR} is the G-R lifetime, and $d(V)$ is the depletion width as a function of the applied bias.

3. The Zener tunneling current occurs when an electron tunnels directly through the effective bandgap without the use of a trap state and can

be written as

$$J_{ZT} = \frac{e^3 F(V) V}{4\pi^2 \hbar^2} \sqrt{\frac{2m_T}{E_g}} exp\left(-\frac{4\sqrt{2m_T E_g^E}}{3e\hbar F(V)}\right) \tag{2.11}$$

where E_g is the effective bandgap energy of the T2SL system, m_T is the tunneling mass, and F is the electric field.

4. Trap-assisted-tunneling (TAT) is similar to Zener tunneling in that it occurs when an electron tunnels through the effective bandgap of the T2SL system. However, while Zener tunneling is simply directly through the bandgap, trap-assisted-tunneling (as its name implies) requires the use of a trap state, either an impurity or defect, with an energy level located in the middle of the bandgap. The (TAT) current can be written as

$$J_{TAT} = \frac{e^2 m_T V M^2 N_t}{8\pi\hbar^3} exp\left(-\frac{4\sqrt{2m_T(E_g - E_t)^3}}{3e\hbar F(V)}\right) \tag{2.12}$$

where N_t is the activated trap density, M^2 is the trap potential matrix element ($\simeq 1\times 10^{-23}$ eV^{2}cm^3 [26]), and E_t is the trap energy.

As mentioned above, T2SLs are limited by trap-assisted-tunneling currents at temperatures below 50 K, generation-recombination (specifically Shockley-Read-Hall [SRH]) currents from T = 50 K to T $\simeq$85 K, and diffusion currents above 85 K. It is possible to confirm this temperature dependence through the use of an Arrhenius plot. In an Arrhenius plot, the R_0A product is plotted on a semi-logarithmic scale versus $1000/T$, where T is the temperature in K. The change of the R_0A product occurs mainly because of the temperature dependence of the intrinsic carrier concentration, which can be written in terms of the temperature and the effective bandgap E_g as

$$n_i^2 \propto exp\left(-\frac{E_g}{k_B T}\right). \tag{2.13}$$

The resulting graph will have groups of points that can be connected by a straight line whose slope corresponds to the activation energy of the dark current mechanism that is dominant at that temperature [23].

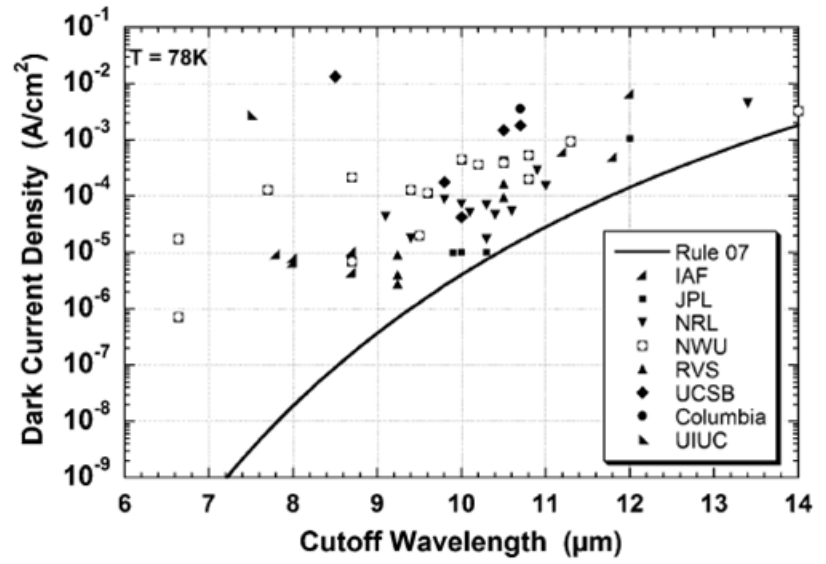

Figure 2.2: Graph of the dark current density vs. λ_{cutoff} for recently published T2SL devices from various institutions structures compared to the current MCT device performance trend (black line). From [27].

2.3 State-of-the-Art for T2SLs

Over the past few years, T2SL performance has been steadily increasing towards the level of the commercially available MCT systems due to better growth quality, fabrication and passivation techniques, and novel layer designs. Figure 2.2 is a plot of the dark current density vs. λ_{cutoff} for some recently published T2SL devices (shapes) and the current MCT performance trend known as the Rule 07 heuristic (black line) [27]. It is clear that MCT still has, in most cases, an order of magnitude or more reduction in dark current compared to the most competitive T2SL structures, though the increase in performance of T2SLs since their inception is encouraging and keeping interest alive in the material system for infrared detection applications.

It may seem strange that interest in T2SLs is so strong even after decades of research with no devices that perform better than their MCT counterparts at any wavelength in the MWIR to VLWIR, yet there is a very simple explanation: simple, nonbarrier T2SLs have been predicted to have a dark current almost two orders of magnitude lower than MCT detectors, as shown in Figure 2.3. However, it is important to note that the state-of-the-art nonbarrier T2SL devices are SRH limited and the theoretical performance improvement assumes that the minority carrier lifetimes in T2SLs will one day be Auger

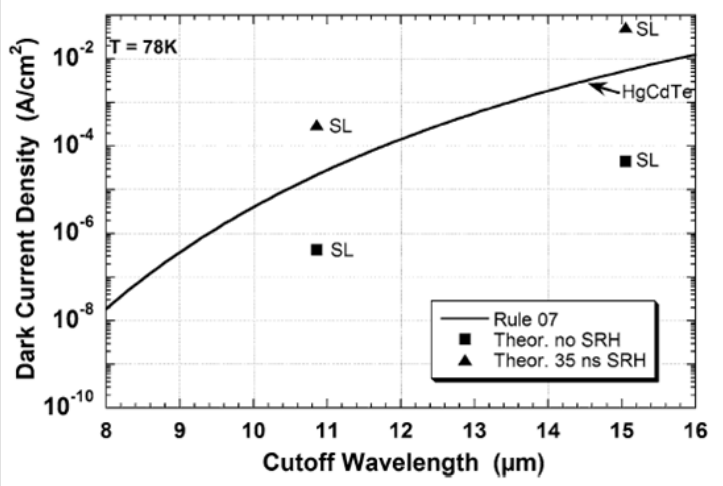

Figure 2.3: Graph of the predicted dark current density vs. λ_{cutoff} for a LWIR and VLWIR nonbarrier T2SL device at 78 K compared to the current MCT device performance trend (black line). T2SLs are currently limited by Shockley-Read-Hall (SRH) defects which, if they persist in device growth, will prevent T2SLs from ever surpassing MCT performance (triangles). However, if the T2SLs are not (SRH) limited (squares) their predicted dark current drops almost two orders of magnitude below that of the state-of-the-art MCT detectors. From [27].

limited [28].

At this point, novel layer structures and passivated diodes are leading the charge towards the state-of-the-art MCT systems. In nearly all cases, the novel layer structures incorporate barriers to either reduce or block dark current. The blocking of carriers reduces the diffusion dark current while the reduction of G-R and trap-assisted-tunneling currents is achieved by placing wide bandgap barriers in the depletion region. Since G-R and TAT dark currents occur in the depletion region itself, a wide bandgap takes advantage of the fact that both of these current mechanisms have terms such as

$$J \propto exp\left(-CE_g\right) \tag{2.14}$$

where C and α are constants. Therefore, an increase in the bandgap of the depletion region will serve to exponentially decrease the G-R and TAT dark currents.

Although T2SL structures that incorporate barriers are prevalent, conventional T2SL structures are still making progress. A 2007 paper [29] demonstrated that increasing the absorber region width in a p-π-n structure, where

π indicates a lightly p-doped absorber region, can lead to a maximum theoretical external quantum efficiency of 78% with an antireflective coating. In fact, by using an absorber region width of 6 μm, an external quantum efficiency of 54% was achieved for a detector with a cutoff wavelength of approximately 12 μm. The results also demonstrated that the dark current density was unaffected as the absorber region width was changed from 1 μm to 6 μ which the external quantum efficiency increased dramatically, indicating that high-quality conventional T2SL layer growth can optimize both the R_0A product and the external QE separately.

2.3.1 W-Structure and Graded-Gap W-Structure

Unlike conventional T2SL layer structures that simply use InAs/GaSb or InAs/InGaSb layers, the W-structure T2SL, first proposed for use in an infrared detector in 2005 by a group at the Naval Research Laboratory (NRL) [30], places a layer of the wide bandgap semiconductor AlSb into each period of the superlattice. The AlSb layer is inserted in the middle of the InAs layer, breaking the electron confining layer into essentially a double quantum well with the wide bandgap AlSb on the outside and the smaller bandgap InGaSb, which confines the holes, on the inside as in Figure 2.4. This serves to increase the electron and hole wavefunction overlap, thereby increasing the optical matrix element and absorption coefficient.

The main advantage of the W-structure is actually the shift of the electron density of states from 3-dimensional to 2-dimensional due to the strong confinement by the AlSb layers. Since the 3-dimensional density of states is proportional to $\sqrt{E_g}$ and the 2-dimensional density of states is a Heaviside step-function, this indicates that the absorption curve for the W-structure is much sharper near the band edge, leading to higher peak quantum efficiencies when compared to T2SLs of the same, or even smaller, cutoff wavelengths. In 2006, the same NRL group produced a W-structure T2SL with a cutoff wavelength of 11.3 μm that could operate at 80 K with an R_0A product of 10–20 Ωcm^2 and an external QE of 34% at 8.6 μm [31]. The design improved upon the first proposed W-structure by replacing the AlSb layers with $Al_{0.4}Ga_{0.49}In_{0.11}Sb$, which has a smaller bandgap than AlSb (but still large enough to confine the electrons) in order to increase the minority-carrier

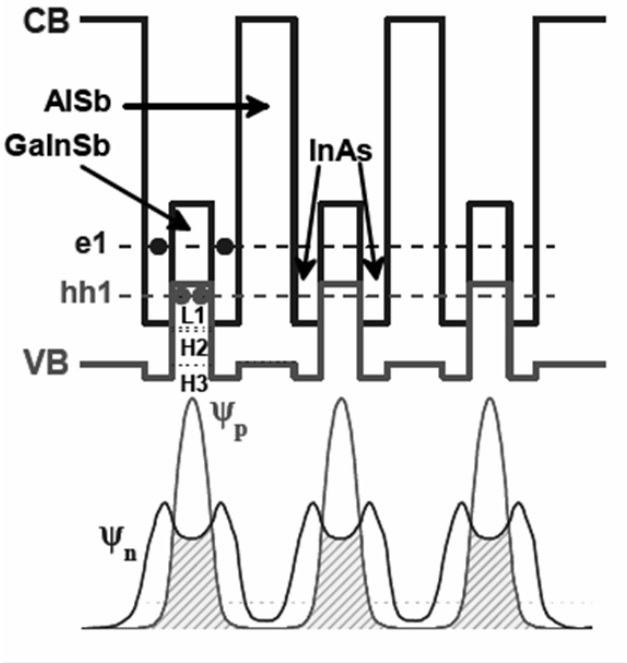

Figure 2.4: Band alignment of the W-structure T2SL material system, which inserts an AlSb barrier layer in the middle of the InAs electron confining layers, forming a double quantum well (top). The AlSb layer serves to further confine the electrons and simultaneously increase their wavefunction overlap with the holes confined in the GaSb layers (bottom), increasing the optical matrix element and, therefore, the absorption coefficient. From [30].

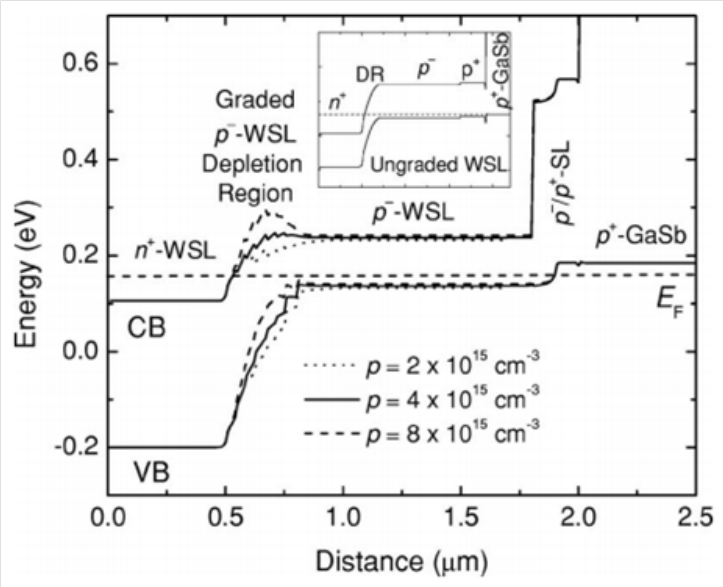

Figure 2.5: Band alignment of the W-structure T2SL material system (inset) compared to the graded W-structure, which reduces the G-R and TAT dark currents by steadily increasing the bandgap of the T2SL in the depletion region. From [32].

mobility and improve collection efficiency.

The graded-gap W-structure maintains the same initial performance metrics as its W-structure predecessor but improves upon them greatly by taking advantage of the exponential dependence on the bandgap of the G-R and TAT dark currents. Shown in Figure 2.5 are the band profiles for the ungraded W-structure (inset) and graded W-structure [32]. The absorber region doping and bandgap remain the same, but the difference arises in the depletion region and n^+ region bandgap. Just before the depletion region, the conduction-band offset is slowly increased in subsequent periods of superlattice until it reaches a value much larger than the absorber region bandgap. Despite the change, the majority of the built-in electric field between the p-n junction falls across the larger bandgap areas, serving to greatly reduce the G-R and TAT dark currents. Another interesting caveat is that the graded bandgap in the depletion region actual serves to self-passivate the device. Since smaller bandgap materials are more easily subjected to surface channel currents due to band-bending and Fermi-level pinning, widening the bandgap serves to decrease these surface tunneling currents, increasing the sidewall resistivity. Using the graded W-structure, R_0A values of approximately 216 Ωcm^2 were

reported at a temperature of 78 K for a cutoff wavelength of 10.5 μm, an increase of over an order of magnitude from the previously mentioned non-graded W-structure.

2.3.2 M-Structure

The M-structure T2SL, first proposed for infrared detection in 2007 by the Razeghi group at Northwestern University [33], is very similar to the W-structure T2SL in that it places a wide bandgap AlSb layer into each period of the layer structure. However, unlike the W-structure, the M-structure places the AlSb layer in the middle of the hole confining GaSb layer, shown in Figure 2.6. The first reason for doing this is a practical one: AlSb and GaSb share a common Sb atom, meaning interfacial layer control between the two materials is much less demanding than when growing AlSb on InAs, or vice versa. Second, the M-structure can be grown using only binary semiconductor materials, unlike the W-structure mentioned above which is grown with both ternary and quaternary alloys, leading to better material uniformity and less-stringent growth conditions. The creation of a double quantum well for holes means that the position of the hole energy levels becomes more sensitive to the individual well widths than in a simple InAs/GaSb superlattice. In fact, the first heavy-hole valence band level can be tuned more than 150 meV from its initial level by changing the width of the AlSb barrier, meaning an effective dark current barrier can be created in the depletion region of the *p*-*n* junction [34]. Finally, the AlSb barrier actually shields the interactions between the electrons in neighboring InAs layers, which increases the electron effective mass and decreases the probability of tunneling (reducing the dark current). For a device with a cutoff wavelength of 10.5 μm at a temperature of 78 K, R_0A products of 200 Ωcm^2 were reported for unpassivated diodes [34].

2.3.3 Complementary Barrier Infrared Detector (CBIRD)

The complementary barrier infrared detector (CBIRD) was introduced for LWIR detector operations in 2009 by a group at the Jet Propulsion Laboratory [35]. The CBIRD operates under the principle of unipolar barriers,

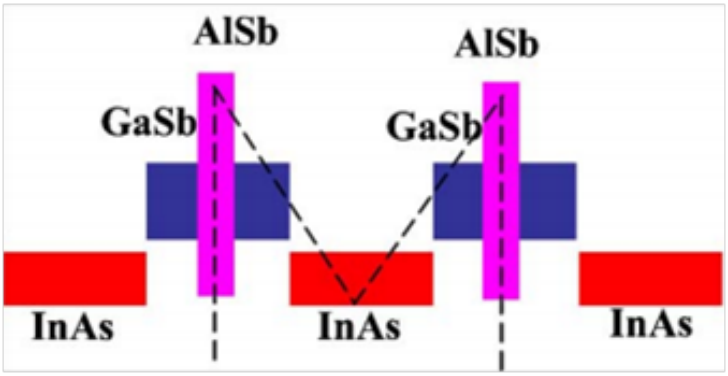

Figure 2.6: Band alignment of the M-structure T2SL material system which inserts a wide bandgap AlSb layer into the hole confining GaSb layer of the T2SL. This serves to increase the electron effective mass (reducing tunneling currents) and allows for easier valence band level tuning without sacrificing much of the electron-hole wavefunction overlap. From [33].

which can block the flow of either electrons or holes in one direction while allowing the other type of hole to flow. These types of barriers are used to block the flow of diffusion dark current by blocking the majority carrier in the superlattice layer structure (holes in p-type and electrons in n-type). The unipolar barriers also offers the benefits described in the M- and W-structure sections above if placed in the depletion region, reducing the G-R and TAT dark currents. Another major advantage of the CBIRD is that it can be grown using only conventional T2SL layer structures. Looking at the band structure in Figure 2.7, taken from [35], the absorber region is composed of InAs/GaSb (44 Å, 21 Å), the electron barrier (eB) superlattice is composed of InAs/GaSb (22 Å, 21 Å), and the hole barrier (hB) superlattice is composed of InAs/AlSb (46 Å, 12 Å), resulting in a much more simplistic design than the M- and W-structures. However, it is important to note that the barriers must be nearly lattice matched to the substrate and the valence and conduction band offsets need to be carefully designed so as to not impede the flow of the photogenerated current. To date, the CBIRD has achieved a 78 K R_0A product of 14 kΩcm^2 for a 9.9 μm cutoff detector, making it the highest of any non-passivated T2SL device.

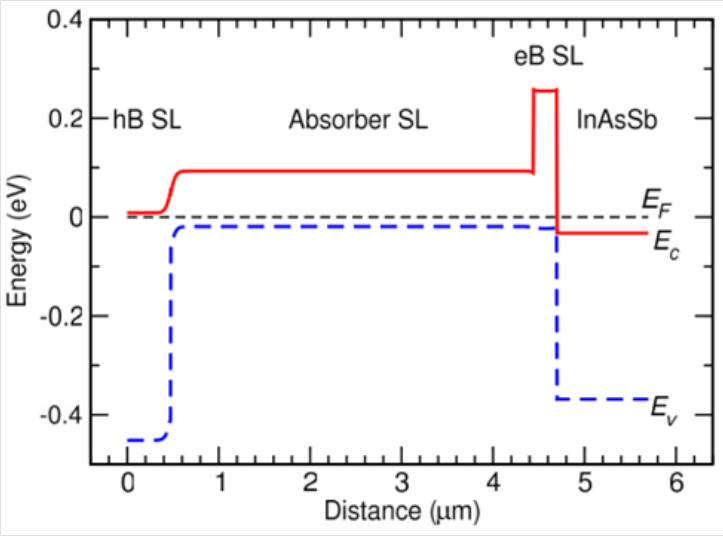

Figure 2.7: Band structure of a complementary barrier infrared detector (CBIRD) which utilizes unipolar barriers to block the diffusion dark current of majority carriers in the superlattice. The electron barrier (eB) is located on the right and the hole barrier (hB) on the left. This CBIRD structure has demonstrated the highest non-passivated performance to date, with a 78 K R_0A product of 14 kΩcm^2 for a 9.9 μm cutoff detector. From [35].

2.4 Summary

Though the state-of-the-art for T2SLs has been slowly approaching that of commercially available MCT detectors over the past decade, there is still much room for improvement in both the growth and fabrication of T2SL devices. It is apparent that novel layer structures that utilize barriers and wide bandgap materials in the depletion region are necessary for higher performance devices, though passivation, which will be discussed in Chapter 6, is another technique used to decrease the surface leakage dark current, which can be quite debilitating if not properly controlled. However, there are other methods that can be employed to decrease the dark current and increase carrier lifetimes, including careful design and control of interfacial layers [14] and utilization of uncommon semiconductor materials [25]. Another potential option is T2SL growth by metal organic chemical vapor deposition (MOCVD), which will be discussed in Chapter 4, though molecular beam epitaxy (MBE) growth currently offers the best control of the thin layer widths needed for the superlattices.

CHAPTER 3

FABRICATION AND CHARACTERIZATION

3.1 Fabrication

3.1.1 Wet Etch Fabrication

There are two main methods used to fabricate T2SL mesas for characterization and Figure 3.1 presents a simple flow chart for the fabrication of a mesa using either method. The first is through the use of a chemical wet etchant, which has the advantage of being simple to set up and monitor, along with requiring very little equipment. One disadvantage is that the chemical solution etches the wafer isotropically. The isotropic etch can undercut the mask used to define the mesa area, leading to devices with smaller total areas than expected and highly sloped sidewalls, such as in Figure 3.2. For single device measurements the sidewall slope can be ignored but much more care is needed if using wet etching to fabricate a focal plane array (FPA), where each device is only tens of microns from its neighbors, or if fabricating devices that have small feature sizes. In the case of this work, the smallest mesa size fabricated was 150 μm $\times$ 150 μm, which is large enough to ignore the issue of size.

After the samples are cleaved from the initial wafer and cleaned using acetone and isopropyl alcohol (IPA), an etching mask is defined using photoresist (PR). The PR acts as a protective barrier from the chemical solution used to etch the T2SL and defines multiple mesas of sizes 400 μm $\times$ 400 μm, 300 μm $\times$ 300 μm, 200 μm $\times$ 200 μm, and 150 μm $\times$ 150 μm. The different sizes allow for a study of device performance (both electrical and optical) in terms of perimeter-to-area ratio (P/A). After the PR mask is defined, the sample is etched using a solution of citric acid monohydrate, deionized water (DI), hydrogen peroxide (H_2O_2), and phosphoric acid (H_3PO_4). The GaSb

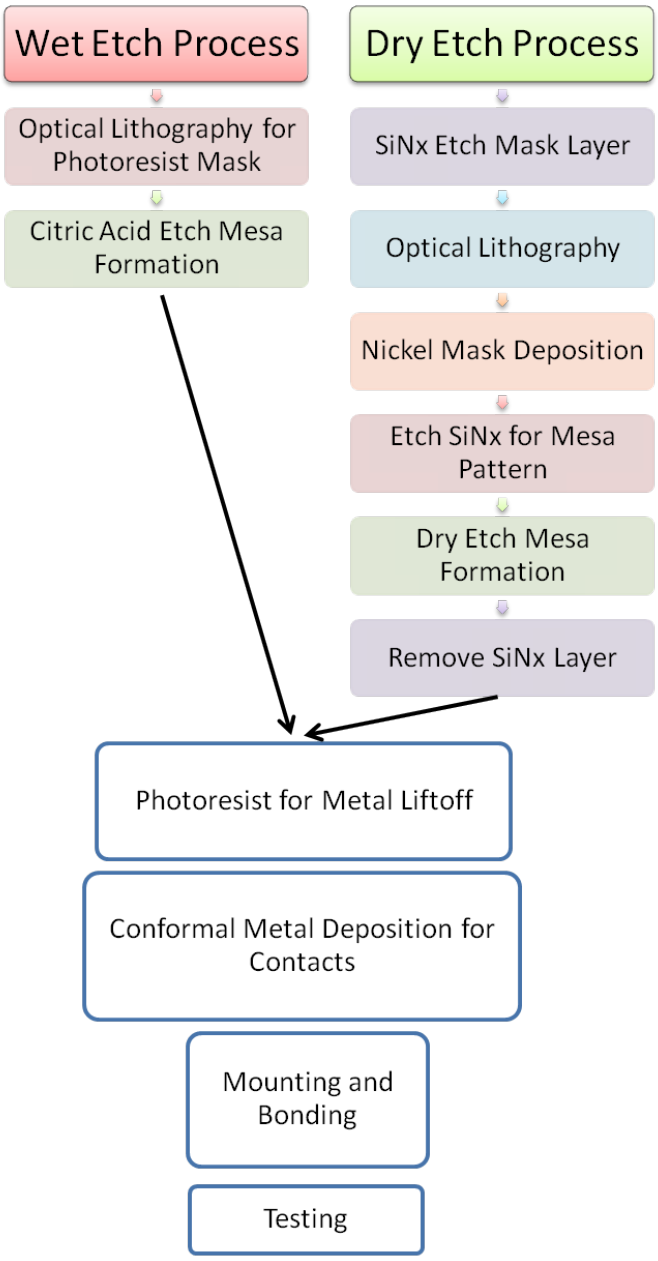

Figure 3.1: Flow chart of the wet etch and dry etch methods that are used to fabricate T2SL mesas. It is easy to see that the wet etch process is much more simple than the dry etch process, though it does have some disadvantages when it comes to device performance, making dry etching the preferred method in the industry.

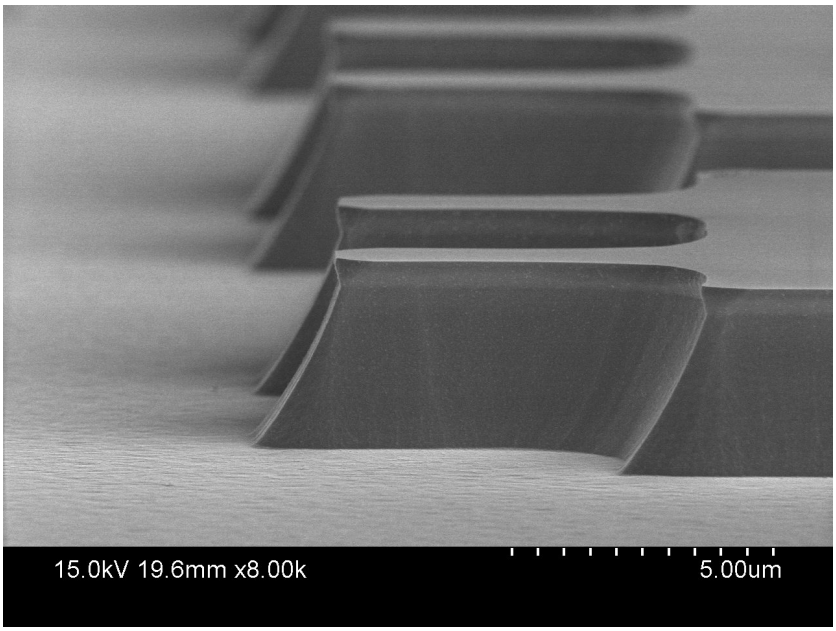

Figure 3.2: Scanning electron microscope (SEM) image of the sidewall of a T2SL alignment mark, etched using a wet etch solution. The sloping sidewall is a result of the isotropic etch that occurs when using the wet solution process. The device is now ready for the second photolithography step and then metal contact deposition.

layers are etched by the phosphoric acid, the InAs layers are etched by the citric acid (the combination of citric acid monohydrate and DI), while the hydrogen peroxide serves as an oxidant. Depending on the accuracy of the measurements, as well as the size of the individual layers in the T2SL, which vary by sample, the etching rate can fluctuate between different batches of the wet etch solution. Thus, it is always important to measure the height of the mesa at different times throughout the etch. This could either be done using an alpha stepper – a surface profilometer that can reach sub-nanometer resolution by scanning a stylus along the top of the sample – or a scanning electron microscope (SEM).

All T2SL samples that are grown for the purpose of device fabrication have a highly doped buffer layer, typically with a width of a few hundred nanometers, between the substrate and the T2SL layers. This is to provide a nearly metallic region for photogenerated carriers to flow and be collected at the bottom contact; therefore, it is important that the wet etch is stopped in this buffer layer or the device performance will be negatively impacted and yield inaccurate and unexpected results.

After the etching is complete, the PR that defines the etching mask is removed and the sample is thoroughly cleaned to remove any etching byproducts or remaining PR and to prepare the sample for contact deposition. As mentioned in Chapter 2, etching or mask byproducts can lead to large surface leakage currents, so it is important to ensure their complete removal from the sidewalls of the device. A second PR step was conducted in the same manner as the first, though using a different mask pattern for depositing the metal contacts. After photolithography, a contact layer of titanium/platinum/gold is deposited by e-beam evaporation and then the remaining PR is stripped, leaving ohmic contacts on top of the mesa itself and on the buffer layer at the bottom of the mesa. Special care must be taken when designing the mask for this contact layer, as the top contact needs to be large enough to have good electrical contact, but small enough to allow a sufficient amount of uncovered mesa for optical measurements.

Finally, the samples are cleaned again and mounted to a ceramic chip carrier using silver paint (for heat conduction). Mesa and ground contacts are then formed between the sample and the chip carrier using a ball bonder, which allows for relatively simple electrical characterization.

3.1.2 Dry Etch Fabrication

The second method used to fabricate T2SL photodetectors is dry etching. As its name implies, it forgoes the use of a chemical solution to etch the mesa, instead using bombardment of reactive ions to blast any uncovered T2SL surface away. Though the process sounds more destructive than wet etching, using a careful combination of gases, plasma powers, temperature, and ion acceleration, dry etching can actually produce sidewalls that are of better quality than those produced via wet etching [36]. Though the machinery and recipes required are far more complex than what is needed for wet etching, once the dry etching procedure has been established it is much faster and provides a much more anisotropic etch. The anisotropic etch leaves very straight sidewalls, seen in Figure 3.3, allowing for higher fill factor FPAs and making dry etching the preferred method in the industry.

The dry etch process occurs at much higher temperatures than the wet etch process, meaning that photoresist is no longer suitable as an etching

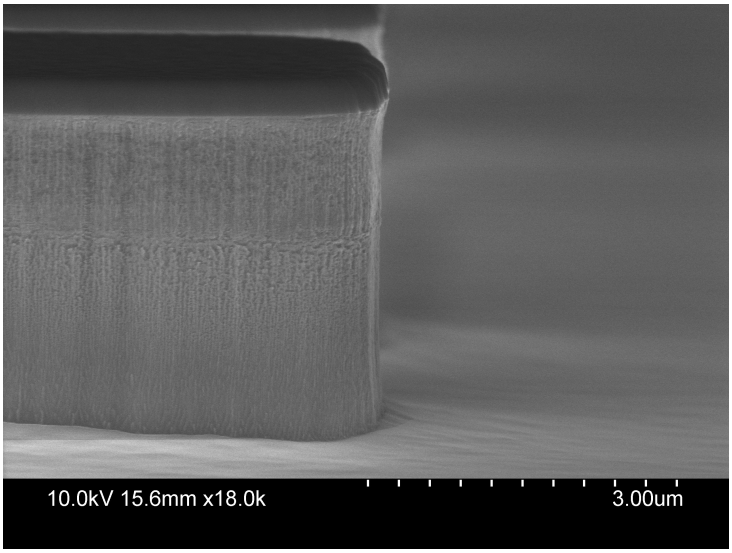

Figure 3.3: Scanning electron microscope (SEM) image of the sidewall of a T2SL alignment mark, etched using a dry etch process. The sidewall is much straighter than when using a wet etch, a result of the anisotropic etch that occurs when using dry etching. The dark layer on the top of the mesa is the silicon nitride (SiN_x) used to define the etching patter, which will be removed to allow for metal contact deposition.

mask because it will burn and cure, becoming extremely difficult to remove. However, PR is still used to define patterns for other steps in the process. After the samples are cleaved from the initial wafer and cleaned using acetone and isopropyl alcohol (IPA), approximately 750 nm of silicon nitride (SiN_x) is deposited on the top of the sample using plasma enhanced chemical vapor deposition (PECVD) to serve as the etching mask for the process. Next, a photolithography step is performed to define the mesa areas. However, the PR is not used as the mask for the removal of the SiN_x. Instead, a 15 nm layer of nickel is deposited using e-beam evaporation, which will serve as the mesa mask for the SiN_x. The transfer of the mask pattern onto the PR can be slightly jagged, especially if good contact is not made between the mask pattern and the PR during the photolithography step. Since dry etching is very precise, any rough or jagged edges will translate directly into the etch of the SiN_x itself and then to the mesa, resulting in bad sidewall quality. However, if a nickel mask is used these problems are avoided.

After nickel deposition the PR is removed and the SiN_x is etched using reactive ion etching, where it is bombarded with ions while simultaneously reacting with other plasmas. The nickel is then stripped using a commercially

available nickel etchant, leaving a SiN_x mask pattern on the top of the sample. The mesa is then etched by a process known as inductively coupled plasma reactive ion etching (ICP RIE). A boron trichloride (BCl_3) and argon (Ar) gas mixture is used and a plasma is generated using a high-frequency electric field. A DC voltage is applied vertically along the plasma chamber, which accelerates the plasma ions towards the surface of the sample and removes any portions not covered by SiN_x (though it is important to note that the SiN_x itself is etched as well, just at a much lower rate) either through the transfer of kinetic energy or a chemical reaction. After the etch is finished, the SiN_x is removed through the use of an RIE, and the sample is cleaned and mounted in a ceramic chip in the same manner as in the previous section.

In both the wet etch and dry etch fabrication processes, the contact metal layer consists of a thin layer of titanium (Ti), platinum (Pt), and a thicker layer of gold (Au). Ti, unlike Pt or Au, adheres very well to nearly all semiconductors, while the Pt and Au are used form ohmic top and bottom contacts. The mesa geometries in this case are simple squares of sizes 400 μm $\times$ 400 μm, 300 μm $\times$ 300 μm, 200 μm $\times$ 200 μm, and 150 μm $\times$ 150 μm, though other geometries can be used.

3.2 Characterization

Samples are mounted on a cold finger and the pins on the ceramic chip carrier are soldered to the internal wiring of a Janis cryostat, which permits the use of both liquid helium and liquid nitrogen experiments, allowing for a range of testing temperatures from 4 K to 300 K. The cryostat is equipped with zinc selenide (ZnSe) windows to permit the transmission of radiation up to 22 μm.

3.2.1 Electrical

The current-voltage (IV) curves are measured using an HP 4145B Semiconductor Parameter Analyzer. The R_0A product can be calculated from this curve by using Equation 2.2. To prevent any background radiation from entering the cryostat during the measurement, aluminum foil is wrapped around to cover each window to ensure the only carriers generated are from thermal

effects. The cryostat cold finger contains a built-in heater that can be controlled very precisely by a Lake Shore 331 Temperature Controller (TEC). This means that the temperature of the sample can be increased or decreased to any desired value between 4 K and 300 K when conducting experiments with liquid helium that is being delivered through a transfer line through the top of the cryostat. Liquid nitrogen experiments cannot be controlled with the TEC due to the lack of a proper Dewar and transfer line; therefore, they must be conducted at 78 K only.

3.2.2 Optical

The optical characterization of the T2SL devices is conducted using an ABB Bomem DA-8 Fourier Transform Infrared Spectrometer (FTIR). Since the wavelengths needed to test the devices fall in the MWIR and LWIR, an FTIR is a popular tool due to the fact that it can use a non-tunable light source, whereas most other techniques require a tunable light source, something that is extremely hard to come by for these longer wavelengths.

The principle of an FTIR is simple and based on the Michelson interferometer shown in Figure 3.4. A broadband source (labeled Source in the figure) – either quartz or Globar in this case – is directed onto a beamsplitter at the point O. Half of the beam is transmitted to a fixed mirror (F) and the other half is transmitted to a movable mirror (M). The beam from the fixed mirror travels back to the beamsplitter where it passes through unimpeded and recombines with light reflected off the beamsplitter from the movable mirror. The light is then focused on the T2SL detector sample, producing a photocurrent. However, the moving mirror creates a path length difference, δ, resulting in either constructive or destructive interference at the T2SL sample. The measured intensity of the T2SL is given by

$$I(\delta) = \int_{-\infty}^{\infty} d\nu B(\nu) cos(2\pi\delta\nu) \tag{3.1}$$

where ν is the wavenumber (λ^{-1}) and $B(\nu)$ is the absorption spectrum of the T2SL, which is calculated through the use of a Fourier transform [37] to be

$$B(\delta) = \left| \int_{-\infty}^{\infty} d\delta I(\delta) exp(-2i\pi\delta\nu) \right|. \tag{3.2}$$

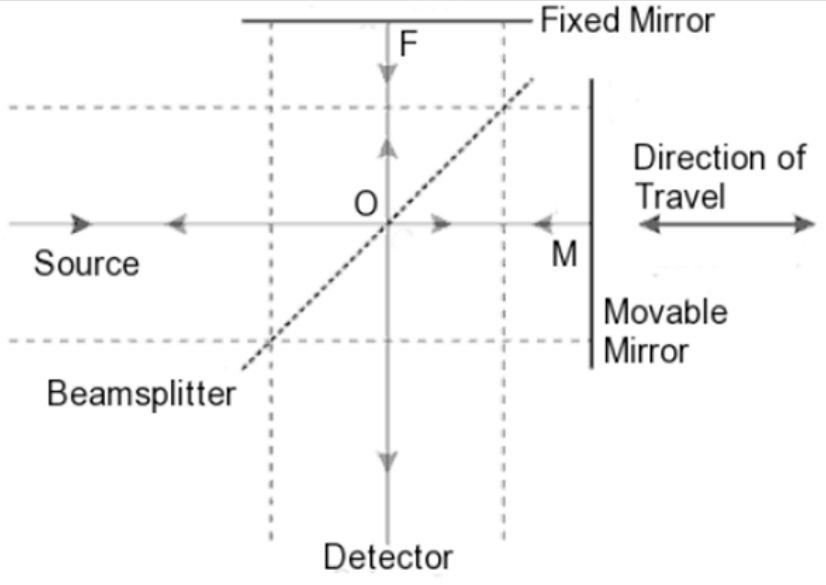

Figure 3.4: The Michelson interferometer inside the FTIR that is used to test the optical response spectrum of the T2SL devices. The beam width is given by the dashed lines while the rays indicate the center of the beam. From [38].

In order to produce the response spectrum of the T2SL, the cryostat is placed at the focal length of the beam emitted by the DA-8. In order to pass radiation wavelengths in the MWIR and LWIR through the internal optics to the device, a KBr beamsplitter is used, along with the built-in Globar source. Using a resolution of 4 cm^{-1} and scanning the mirror 100 times generates the responsivity curve for the T2SL. It is important to note that the number of scans needed is dependent on the quality of the T2SL device being tested: higher quality devices will require fewer scans due to their higher signal-to-noise ratio.

The responsivity curve that is output by the FTIR is in arbitrary units because the FTIR does not have the ability to normalize the data it is generating through the Fourier transform. Therefore, the responsivity curve can only give data about the performance of one device in relation to another on the sample but with no true values for comparison with any other devices. Thus, the data must be calibrated by using the known responsivity of the device in question at a single wavelength. The calibration can be done using a blackbody source, in this case a Mikron M 305, at a temperature of 1273 K. The radiation from this blackbody is first passed through a chopper,

then an aperture, then a spike filter designed for a wavelength of 4.845 μm and the resulting T2SL photocurrent, I_p, can be measured using a current preamplifier and lock-in amplifier.

Based on the approximations that the transmission of the cryostat window is constant around the wavelength of the spike filter and the distance of the T2SL from the blackbody source is much larger than the aperture, the root mean squared power, Φ_d, on the T2SL can be calculated as

$$\Phi_d \cong \pi \left(\frac{a}{2d}\right)^2 A_{opt} c_m t_w \int_{k1}^{k2} \frac{k^3 h c^2}{8\pi^4 (e^{hck/2\pi k_B T} - 1)} t_f(k) dk \tag{3.3}$$

where k is the wave vector, A_{opt} is the optical area of the detector mesa, a is the radiation aperture size, d is the distance from the radiation aperture to the detector, c_m is a constant proportional to the dimensions of the chopper, t_w is the constant response of the cryostat windows, k_1 and k_2 are the spike filter cutoff wavelengths, and $t_f(k)$ is the spike filter response, measured in the FTIR using a commercially available MCT detector.

Once I_p and Φ_d are known, the responsivity of the device can be calculated at 4.845 μm by $R_{4.845\ \mu m} = I_p/\Phi_d$. The resulting value can then be used to calibrate the relative responsivity curve from the FTIR to generate the absolute responsivity curve, which has y-axis units of amperes/watt (A/W).

CHAPTER 4

METAL-ORGANIC CHEMICAL VAPOR DEPOSITION GROWN T2SLS ON AN INDIUM ARSENIDE SUBSTRATE

4.1 Growth and Fabrication

Until just a few years ago [16, 17], T2SLs had been grown by molecular beam epitaxy (MBE) only. III-V MBE growth is a very mature field that offers high-quality growth over large wafer sizes, as well as submonolayer control over layer widths. As mentioned in Chapter 1, this precise width control is extremely important for T2SLs due to the change in cutoff wavelength for even small deviations in layer size. However, the MBE growth of T2SLs is expensive and time consuming due to its slow deposition rates, so a more practical growth method is needed if T2SL technology is to be commercialized in the future. Metal-organic chemical vapor deposition (MOCVD), the preferred growth method in the industry, when available, due to its fast deposition rates with only a minimal sacrifice in growth precision, has recently been demonstrated for a GaSb substrate T2SL [16]. This was the first fabricated and tested T2SL device that had been grown by MOCVD, giving hope to the idea that MOCVD T2SLs could one day compete with their MBE grown counterparts in terms of device performance. However, there are significant challenges involved when growing InAs/GaSb T2SLs via MOCVD. The main difficulty concerns the interfacial (IF) layers. As mentioned in Chapter 1, if there is no intentional strain compensation, the IF layers will randomly be either GaAs-like or InSb-like binary, ternary, or even quaternary alloys. Though the formation of these IF layers is an attempt by the wafer to "self-strain balance", the interface roughness (defects), effective bandgap, and absorption coefficient all depend heavily on the choice of IF layers. The compressive strain caused by the InSb-like IF layers (large lattice constant of 6.479 Å) can actually cause a significant redshift in the cutoff wavelength, while GaAs-like IF layers (smaller lattice constant of 5.65

Å) can cause a large blueshift [14]. Other considerations for the IF layers used are the roughness and abruptness of the interface itself, which need to be reduced and increased, respectively. It has been shown that InSb-like IF layers are not only smoother than GaAs-like layers, but they are also more abrupt (whereas no control of IF layers results in the most diffuse and least desirable interfaces) [3]. In the end, the choice of IF layers is most important for strain balancing the several-μm-thick T2SLs, as the lattice mismatch of the SL compared to the substrate needs to be kept below $\pm 5 \times 10^{-3}$ [3].

When MBE growth is used for T2SL samples on a GaSb substrate, InSb IF layers can be easily incorporated into the design. However, the growth temperatures used during MOCVD are much higher than with MBE and actually approach the melting point of InSb, rendering them almost useless for IF control. The first generation of MOCVD grown T2SLs, performed by Professor Russell Dupuis of the Georgia Institute of Technology, used a complicated IF scheme involving the ternary alloys InAsSb and InGaSb [15] to strain balance the layer structure to the GaSb substrate, making the overall growth of the T2SL extremely difficult. However, this difficulty can be mitigated through the use of an InAs substrate, an uncommon substrate to use for MBE grown T2SLs and one that has never been used for MOCVD grown T2SLs until last year [17]. There are two reasons for using InAs instead of GaSb for the substrate. First, when growing an InAs/GaSb superlattice, the InAs layers are lattice matched but the GaSb layers are compressively strained due to their larger lattice constant. To compensate, GaAs IF layers can be used, greatly reducing the problems that arise when InSb layers are needed but cannot be grown due to the temperature restraints. The second advantage of the InAs substrate is its lower absorption coefficient in the MWIR and beyond when compared to GaSb, as demonstrated in [17]. This improvement is thought to be a result of a reduction in free carrier absorption in the InAs substrate compared to the GaSb substrate. Since most focal plane arrays (FPA) are flip-chip bonded, the substrate needs to be either mechanically lapped or chemically etched to a very thin layer to allow for back-side light collection, which can be a tedious process and potentially damage the sample if done incorrectly. However, the use of an InAs substrate requires much less processing to reach the same level of absorption loss as a GaSb substrate, offering an ideal alternative if it can be proven viable to grow on.

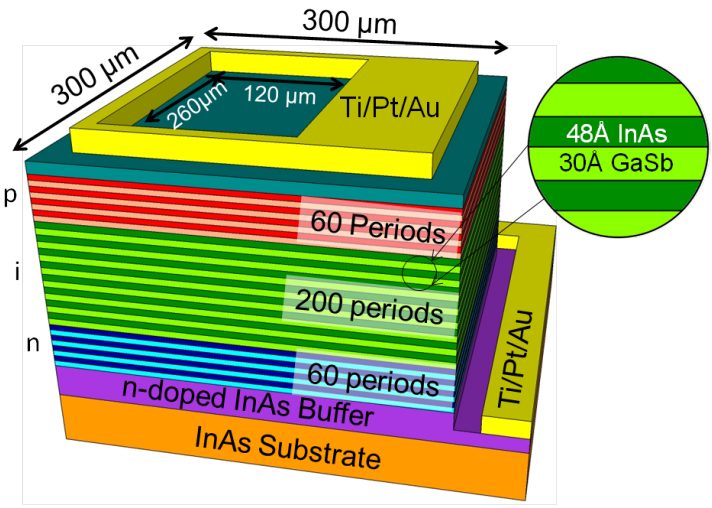

Figure 4.1: Schematic of a 300 μm $\times$ 300 μm detector mesa (not to scale) etched out of the MOCVD wafer 3-2130 (provided by Professor Russell Dupuis at Georgia Tech). 3-2130 is an InAs/GaSb (48 Å, 30 Å) T2SL with a cutoff wavelength of approximately 10.3 μm. In this figure, the wafer has been etched into the highly n-doped InAs buffer layer and ohmic contacts have been deposited on the top of the mesa and the buffer layer.

The sample tested in this work was grown via MOCVD by the group of Professor Dupuis, a pioneer of the growth method, and designated as 3-2130, with a designed cutoff wavelength of approximately 10 μm. The wafer consists of a highly n-doped (1.5×10^{18} cm^{-3}), 300 nm wide InAs buffer layer, grown on a nominally n-type (2×10^{16} cm^{-3}) InAs substrate. Next, the n-i-p superlattice is grown in the following order: 60 periods of graded n-doped (2×10^{18} cm^{-3} to 1×10^{16} cm^{-3}) InAs/GaSb (48 Å, 30 Å), followed by 200 periods of non-intentionally doped InAs/GaSb (48 Å, 30Å), and 60 periods of graded p-doped (1×10^{16} cm^{-3} to 2×10^{18} cm^{-3}) InAs/GaSb (48 Å, 30Å). The structure is capped by a highly p-doped (2×10^{18} cm^{-3}), 50 nm GaSb contact layer.

Devices of 150 μm $\times$ 150 μm, 200 μm $\times$ 200 μm, 300 μm $\times$ 300 μm, and 400 μm $\times$ 400 μm were then fabricated (with a schematic of one such device shown in Figure 4.1), though due to problems during processing only the 300 μm $\times$ 300 μm and 400 μm $\times$ 400 μm were of good enough quality to test.

4.2 Characterization

Electrical characterization of mesas with sizes of 300 μm $\times$ 300 μm and 400 μm $\times$ 400 μm was performed using an HP 4145B Semiconductor Parametric Analyzer, producing current-voltage (IV) curves from which the differential resistance at zero bias product, or R_0A, could be extracted. Measurements were performed using liquid nitrogen at a temperature of 78 K. Figure 4.2 (a) plots the resulting IV curves for 8 different devices, 5 of them 400 μm $\times$ 400 μm (solid lines) in size and 3 of them 300 μm $\times$ 300 μm (dashed lines) in size. One thing that is immediately noticeable is the large dark current. In the reverse bias, an ideal diode will typically have a small, constant current (though real devices will have a slight slope), until reaching its reverse breakdown voltage which permanently damages the device and creates a short circuit. All of the devices tested have rapidly increasing dark current, with the slope increasing until -0.3 V, where the measurement was concluded. Thus, the reverse bias dark current is not only large, it is highly dependent on the bias voltage, and, as the work of Mou et al. [23] has shown, the limiting mechanism is trap-assisted-tunneling (TAT).

Despite there being two different sized devices, it is difficult to tell from the IV curves alone whether there is a trend regarding different mesa areas. However, if the current density is plotted versus the voltage, such as in Figure 4.2 (b), it becomes clear that different sized devices group together in the reverse bias regime, with the 300 μm $\times$ 300 μm (dashed lines) mesas all having larger dark current densities than any of the 400 μm $\times$ 400 μm (solid lines) curves. The same can also be said of the RA, or differential resistance, curves plotted in Figure 4.3. In this figure, the 400 μm $\times$ 400 μm mesas have larger RA products over all voltages, indicating that better performance is directly correlated to device size for this particular fabricated sample. One important thing to note is that the maximum of the RA curves does not occur at zero bias. This is due to the nature of the ideal diode curve, which should have a slope of zero, corresponding to an infinite RA, in the reverse bias. However, these devices are not ideal diodes, so the RA product rises initially then rolls over as the dark current increases exponentially as a function of increasing reverse bias. Despite the fact that the R_0A product is an important figure of merit when discussing detector noise and performance, it should be more intuitive to operate the device at the maximum of the RA curve as

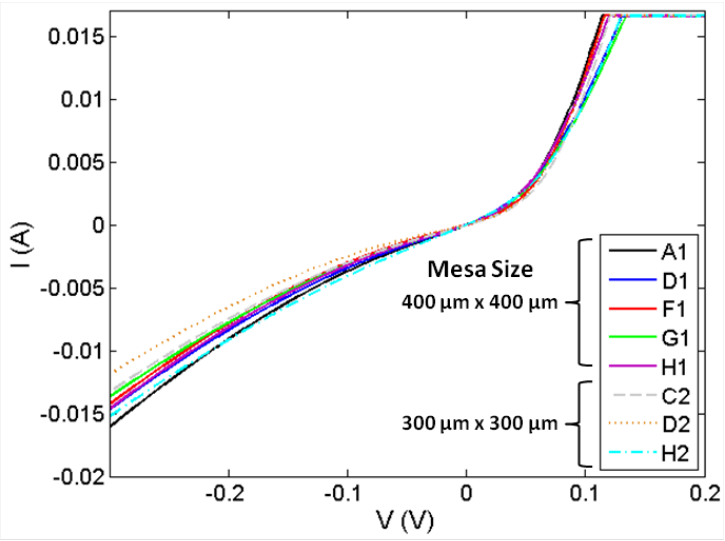

(a)

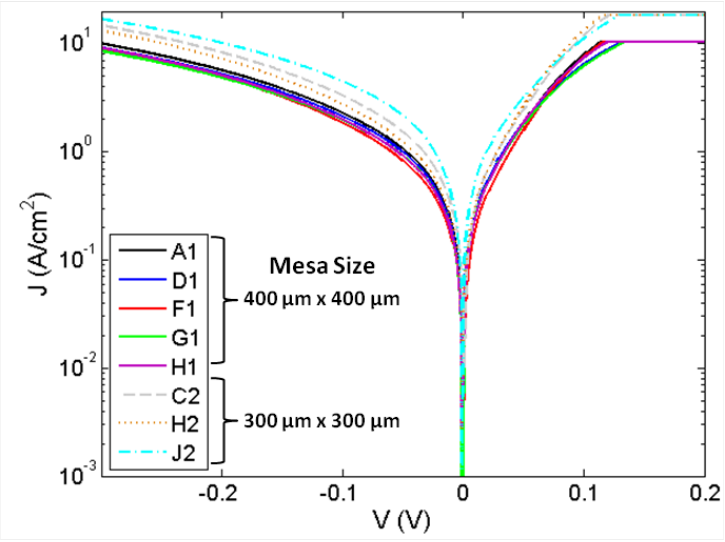

(b)

Figure 4.2: Current-voltage (IV) (a) and current density vs. voltage (JV) (b) curves for 8 MOCVD grown 3-2130 devices for two different mesa sizes: 300 μm $\times$ 300 μm (dashed lines) and 400 μm $\times$ 400 μm (solid lines). The dark current of these MOCVD devices is orders of magnitude larger than state-of-the-art MBE grown T2SL devices.

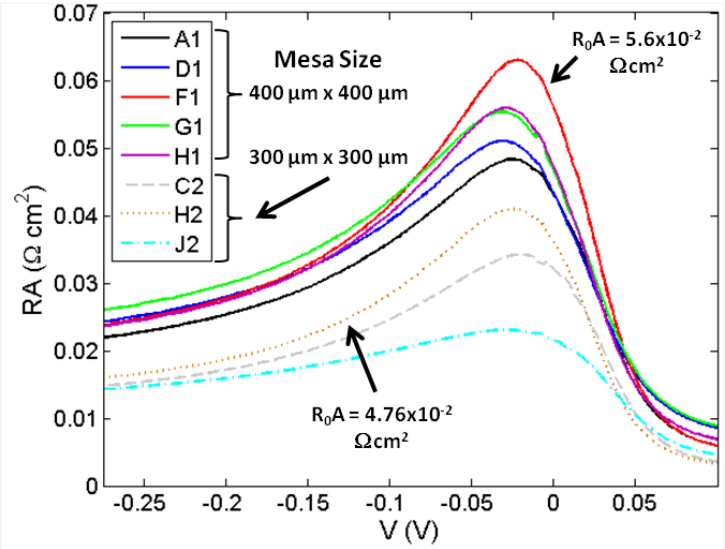

Figure 4.3: RA product curves calculated from the current-voltage curves for 8 different 3-2130 devices. 400 μm $\times$ 400 μm devices are shown with solid lines and 300 μm $\times$ 300 μm devices with dashed. In all cases, the maximum RA value occurs when the devices are slightly reverse biased. The maximum R_0A value measured for a 400 μm $\times$ 400 μm device is 5.6 $\times$ 10^{-2} Ωcm^2 and 4.766 $\times$ 10^{-2} Ωcm^2 for a 300 μm $\times$ 300 μm device.

long as the dark current is sufficiently small. Indeed, some state-of-the-art devices either demonstrate peak RA values near, but not at, the zero bias point [29, 39] and others, such as the CBIRD [35], demonstrate the best performance when slightly reverse biased. The average of the R_0A products is slightly larger than 1.5 times the value of the first generation of MOCVD devices, which were grown on a GaSb substrate, with the largest R_0A of 5.6 $\times$ 10^{-2} Ωcm^2 for a 400 μm $\times$ 400 μm device, exactly 1.4 times larger than the largest GaSb substrate device of the same size [16]. However, the R_0A products are still over three orders of magnitude lower than even the worst performing state-of-the-art device mentioned in Chapter 2, the W-structure. This is to be expected, as 3-2130 is only the second generation of MOCVD grown T2SLs and contained no light p-doping in the absorber region and no barriers or wide bandgap materials.

Table 4.1 gives a summary of the average R_0A product for all measured devices, as well as the standard deviation and perimeter-to-area (P/A) ratio. The P/A ratio is actually very useful when attempting to discern trends between different sized devices. Figure 4.4 plots the individual device inverse R_0A products as a function of their P/A ratio. Equation 2.3 says that the

Table 4.1: Average R_0A products for all the measured devices fabricated from 3-2130, along with the mesa size, perimeter-to-area (P/A) ratio, standard deviation (σ), and total number of detectors measured (N).

Size (μm^2)	**P/A (cm^{-1})**	**Mean R_0A (Ωcm^2)**	**σ (Ωcm^2)**	**N**
(400 μm)^2	100	4.722×10^{-2}	5.26×10^{-3}	5
(300 μm)^2	133.33	3.857×10^{-2}	8.06×10^{-3}	3

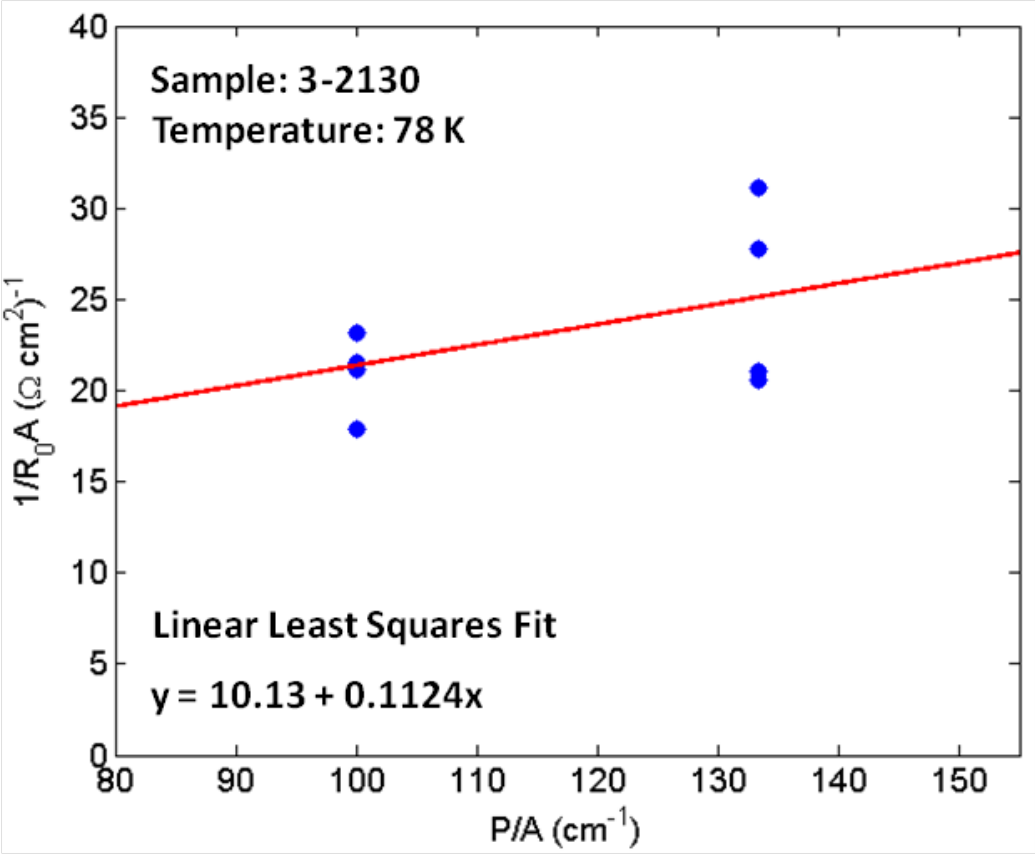

Figure 4.4: Inverse R_0A product plotted versus the perimeter-to-area ratio (P/A). Using a linear least squares fit (solid line) and Equation 2.3 the bulk R_0A product and surface resistivity can be calculated. A constant fit would indicate infinite surface resistivity and no leakage current. However, the slope of the solid line indicates the presence of surface leakage current which becomes more debilitating to performance as the devices become smaller.

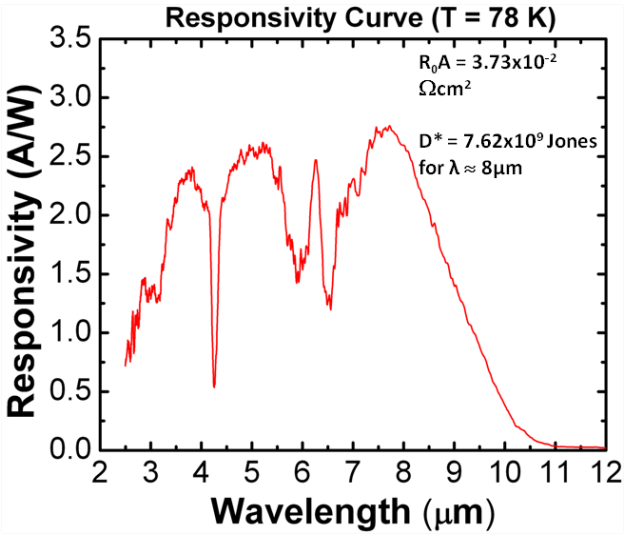

Figure 4.5: The calibrated responsivity curve for a 300 μm $\times$ 300 μm size 3-2130 device. The relative responsivity spectrum was taken at 78 K using an ABB Bomem DA-8 FTIR and then calibrated using a Mikron M 305 blackbody source at a spike filter wavelength of 3.448 μm using the process described in Chapter 3. The peak specific detectivity is 7.62 $\times$ 10^9 Jones at approximately 8 μm, a 4.8 times increase from the value of 1.6 $\times$ 10^9 Jones reported for the first MOCVD grown T2SL on a GaSb substrate in [16].

least squares fit for these points should be linear, with the y-intercept equaling the bulk R_0A product and the slope of the curve equaling the surface resistivity, $\rho_{surface}$. An ideal group of photodetectors would have a linear least squares fit with no slope, implying an infinite surface resistivity and, therefore, zero surface leakage dark current. However, the fit of the 3-2130 devices, with a calculated R_0A_{bulk} of 9.87 $\times$ 10^{-2} Ωcm^2 that agrees well with other InAs substrate MOCVD devices [17], has a slope corresponding to a $\rho_{surface}$ of only 8.9 Ωcm. This is indicative of a large surface leakage current that is negatively impacting the performance of the devices, particularly as they shrink in size. This also explains why different sized detectors group together in the reverse bias regime of Figure 4.2 (b) when all devices should normalize to the same current density: As the device size shrinks, the perimeter-to-area ratio and, therefore, surface leakage current contribution increases, resulting in larger dark current densities. Surface leakage mitigation has always been a problem for infrared detectors, and there have been many attempts to eliminate its contribution, some of which will be covered in Chapter 6.

Figure 4.5 shows the absolute responsivity spectrum for a 300 μm $\times$ 300 μm size device. The relative responsivity spectrum was taken at 78 K using an ABB Bomem DA-8 FTIR and then calibrated using a Mikron M 305 blackbody source at a spike filter wavelength of 3.448 μm using the process described in Chapter 3. One important thing to note about the curve is that the drop off on the left-hand side, from 2 to 4 μm is non-physical in nature. The beam splitter used by the FTIR to reach these wavelength is made of KBr, which starts to absorb heavily as the wavelength decreases below 4 μm. Also, a Globar source was used, which begins to drop off below 4 μm and contributes to the decline in the responsivity curve. The dips in the curve between 5.5 and 7.5 μm are due to water absorption in the atmosphere of the internal optics of the FTIR and in the space between the emission window and cryostat. The dip at approximately 4.25 μm is due to carbon dioxide (CO_2). Both of these contributions can be eliminated by evacuating the internal optics of the FTIR and purging the sample chamber with pure nitrogen gas, though neither of these options were available at the time of the measurements. The peak specific detectivity is 7.62 $\times$ 10^9 Jones at approximately 8 μm, a 4.8 times increase from the value of 1.6 $\times$ 10^9 Jones reported for the first MOCVD grown T2SL on a GaSb substrate in [16]. However, this is still over two orders of magnitude lower than unpassivated MBE grown T2SLs of a similar cutoff wavelength [29]. One other thing to note is that the responsivity of the detector reaches zero at around 10 μm, which agrees nearly exactly with the designed cutoff wavelength of the structure. However, there is still a slight absorption tail that extends out to almost 11 μm. This can be attributed to deformities or imperfections in the crystal structure of the lattice that broaden the density of states at the band edges and slightly decrease the effective bandgap of the T2SL, though providing very little absorption [40].

In the end, it is clear that there is still much work to be done in the design, growth, processing, and post-processing (passivation) of these structures before they can compete with even the unpassivated state-of-the-art MBE grown devices. However, MOCVD T2SL growth is an new field and there are vast areas that can be improved upon to quickly increase the performance of these devices. This chapter detailed just one of those (changing the substrate from GaSb to InAs) though passivation, novel layer structures, and careful control of interfacial layers are but a few of the options available.

CHAPTER 5

THE ELECTRICAL PERFORMANCE OF MOLECULAR BEAM EPITAXY GROWN T2SLS

5.1 Fabrication

As mentioned in Chapter 1, the doping in the many period absorber region of a T2SL is another important factor that contributes to the device performance and must be considered carefully when designing a structure. As it turns out, it is more beneficial to grow T2SLs on a p-type GaSb substrate in the n-on-p configuration, where the absorber region is lightly p-doped, forming a p^+-p-n^+ diode. Looking at the growth direction energy band structures of typical InAs/GaSb or InAs/InGaSb superlattices, the effective mass of holes is much heavier than that of the electrons, making them harder to collect [9]. Thus, it is desirable to have electrons as the minority carriers in the absorber region, hence the light p-doping, which results in not only better vertical transport properties but a further reduction in Auger recombination rates with only a minimal decrease in the wavelength dependent absorption coefficient due to the introduction of extra holes in the VB and no change in cutoff wavelength [14, 41]. In order to test this theory, state-of-the-art MBE grown T2SLs were ordered from IQE based on designs using a modified 8 band $\mathbf{k}\cdot\mathbf{p}$ theory [14]. The wafer consists of a highly p-doped (1.0×10^{18} cm^{-3}), 500 nm wide GaSb buffer layer, grown on a nominally p-type GaSb substrate. Next, the p-p^--n superlattice is grown in the following order: 80 periods of graded p-doped (1×10^{18} cm^{-3} to 2×10^{17} cm^{-3}) InAs/GaSb (45 Å, 24 Å), followed by 300 periods of lightly p-doped InAs/GaSb (45 Å, 24Å), and 80 periods of graded n-doped (2×10^{17} cm^{-3} to 1×10^{18} cm^{-3}) InAs/GaSb (45 Å, 24Å). The structure is capped by a highly n-doped (1×10^{18} cm^{-3}), 20 nm InAs contact layer and a 5 nm undoped GaSb cap layer for protection from the ambient atmosphere.

Two different samples were grown, each with the same layer structure but

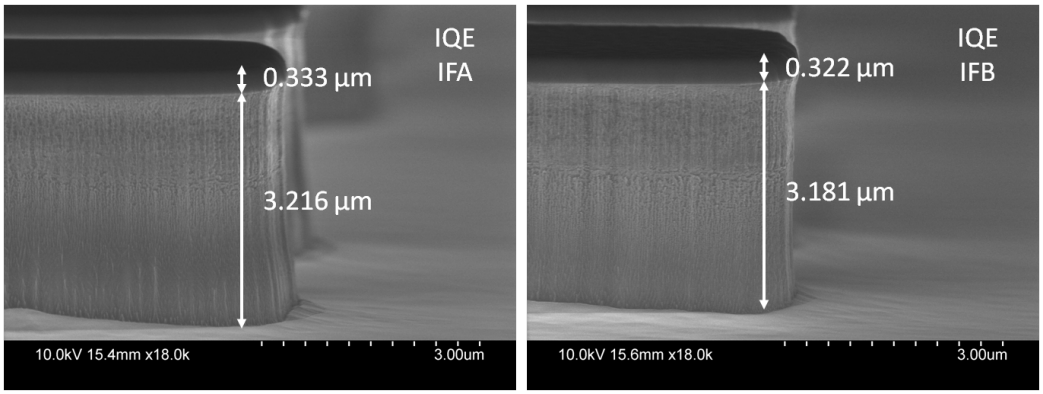

Figure 5.1: SEM images of the sidewalls of two samples fabricated simultaneously by dry etching. On the left is IFA and on the right is IFB. Even accounting for the angle of the SEM, the IFB etch comes to slightly less than the 3.199 μm needed to reach the highly doped buffer layer, which could be the cause of some of the results presented later in the chapter.

different levels of light p-doping in the absorber region. The first sample, labeled in this work as IFA, has an absorber region light p-doping of 5.0×10^{15} cm^{-3} and the second sample, labeled in this work as IFB, has an absorber region p-doping of 1.0×10^{16} cm^{-3}. Devices of 200 μm $\times$ 200 μm, 300 μm $\times$ 300 μm, and 400 μm $\times$ 400 μm were then fabricated using the dry etching fabrication method described in Chapter 3. Figure 5.1 shows SEM pictures of both IFA (left) and IFB (right) after the etching step was completed. The darker area on the top of the mesas is the remaining SiN_x that is used as a dry etch mask. The etching depths for each sample are also shown. Though the devices were etched simultaneously to avoid any ambiguities that may arise if doing separate processes (such as machine status or cleanliness), the IFA etch is slightly larger than the IFB etch. In order to reach the highly doped buffer layer, 3.199 μm must be etched away, meaning that the IFA etch is most likely in the buffer layer while the IFB etch is slightly less, even accounting for the angle in the SEM, which could be a potential cause of some of the results that will be presented later in the chapter.

5.2 Characterization

Electrical characterization of mesas with sizes of 200 μm $\times$ 200 μm, 300 μm $\times$ 300 μm, and 400 μm $\times$ 400 μm was performed using an HP 4145B

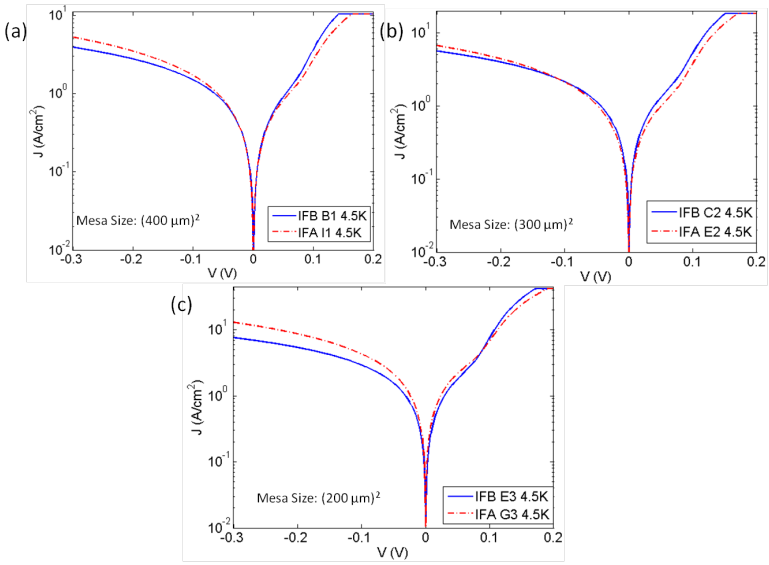

Figure 5.2: Comparison between IFA (dashed) and IFB(solid) JV curves for different sized devices, 400 μm $\times$ 400 μm (a), 300 μm $\times$ 300 μm (b), and 200 μm $\times$ 200 μm (c), at a temperature of 4.5 K. In all cases, the reverse bias dark current density is less for IFB than IFA, which is to be expected due to the higher p-doping in the absorber region of the IFB sample. However, there is still significant surface leakage current present, as evidenced the increasing dark current density with decreasing device size.

Semiconductor Parametric Analyzer, producing current-voltage (IV) curves from which the R_0A product could be extracted. However, as mentioned in Chapter 4, it is more beneficial to plot the current density vs. voltage curves. Figure 5.2 plots the JV curves for different sized IFA (dashed) and IFB (solid) curves. As predicted, the IFB devices perform better regardless of device size in the reverse bias, as can be seen when looking at V $= -0.3$ volts for the 400 μm $\times$ 400 μm (a), 300 μm $\times$ 300 μm (b), and 200 μm $\times$ 200 μm (c) curves, which were taken at a liquid helium temperature of 4.5 K. However, the 300 μm $\times$ 300 μm IFA curve shows slightly better performance than IFB at reverse bias voltages from 0 to -0.1 volts and the current density at -0.3 volts does not follow the trend set by the two other devices sizes in which the gap between IFA and IFB increases. This is possibly a result of insufficient post-processing cleaning of the IFB sample, leading to a slightly increased surface leakage current. However, as with the MOCVD grown devices presented in Chapter 4, there is a definite surface leakage component of the dark current, as evidenced by the increasing dark current density at -0.3 volts as the size of the devices decreases.

Table 5.1: Surface resistivity ($\rho_{surface}$) and R_0A_{bulk} product calculated for temperatures of 4.5 K, 78 K, and 116 K for samples IFA (top) and IFB (bottom).

Temperature (K)	$\rho_{surface}$ **(Ωcm)**	$\mathbf{R_0A_{bulk}}$ **(Ωcm^2)**
4.6 K	6.01	1.11
78.5 K	4.90	0.584
116 K	2.91	5.87×10^{-2}
4.5 K	6.13	0.749
78.15 K	4.33	0.435
115.1 K	2.47	4.26×10^{-2}

Figures 5.3 (IFA) and 5.4 (IFB) are plots of $(R_0A)^{-1}$ versus the P/A ratio for the three different sized devices tested. The solid line is a linear least squares fit of the data, and using Equation 2.3 it is possible to extract the bulk R_0A product and the surface resistivity. As mentioned in the previous chapter, an ideal detector would have no surface leakage dark current, indicating an infinite surface resistivity. In that scenario, the slope of the best fit line would be zero and the R_0A product of each device would be equal to the bulk R_0A product, which would offer insights into other dark current mechanisms such as G-R and TAT, as well as the growth quality of the T2SLs. However, in both figures, the best fit line has a significant slope, indicative of surface leakage. Figures 5.3 (IFA) and 5.4 (IFB) contain the plots for three different temperatures: 4.5 K (a), 78 K (b), and 115 K (c). As expected, as the temperature increases both the surface resistivity and R_0A_{bulk} decreases. This can be explained by looking at the dark current equations given in Chapter 2, which all contain temperature dependent terms that increase as the temperature increases. Therefore, the R_0A_{bulk} decrease is expected because it is the large increase in bulk dark current that prevents T2SLs from operating at high temperatures. The decrease in surface resistivity is also expected: Mou et al. demonstrated that the surface leakage current is proportional to an $\exp(-1/T)$ term, which increases rapidly with temperature [23]. Table 5.1 gives the calculated R_0A_{bulk} and $\rho_{surface}$ values for each sample and temperature.

There are a few important things to notice about the data contained in Table 5.1. The first is that the surface resistivity at all three temperatures is nearly the same for both samples. Since they were both fabricated simultane-

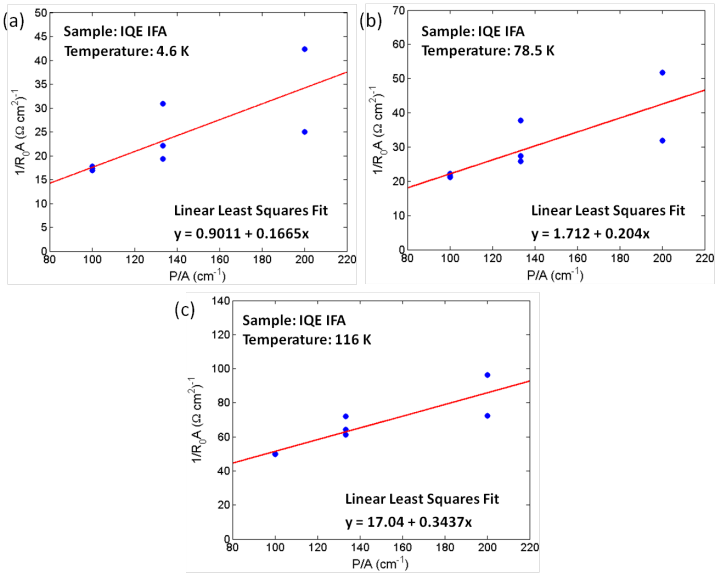

Figure 5.3: Inverse R_0A product plotted versus the perimeter-to-area ratio (P/A) for devices fabricated from sample IFA. Using a linear least squares fit (solid line) and Equation 2.3, the bulk R_0A product and surface resistivity can be calculated. As evidenced by the slope of the line, the surface resistivity is not infinite, which is an indicator of surface leakage current.

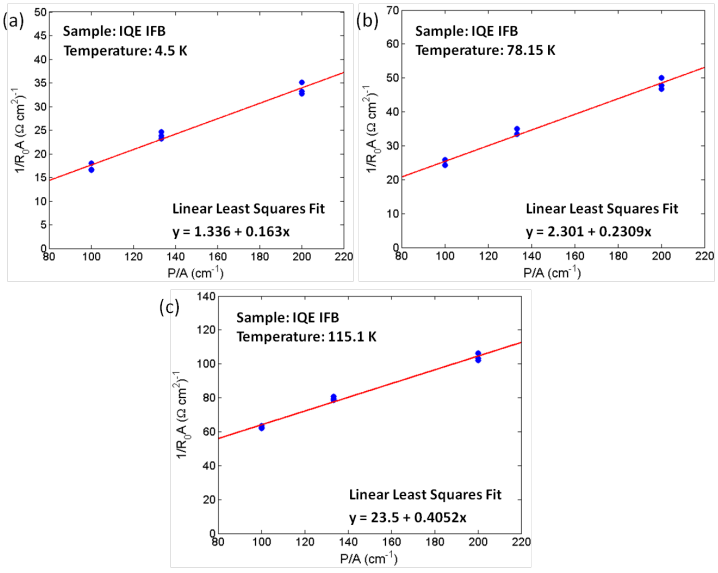

Figure 5.4: Inverse R_0A product plotted versus the perimeter-to-area ratio (P/A) for devices fabricated from sample IFB. Using a linear least squares fit (solid line) and Equation 2.3, the bulk R_0A product and surface resistivity can be calculated. As with the IFA devices in Figure 5.3, the surface resistivity is not infinite, which is an indicator of surface leakage current and results in a slope to the fitting line.

ously, this is expected and is indicative of an unpassivated device. However, the surface resistivity at 78 K is slightly more than half the value of the surface resistivity calculated for the MOCVD grown 3-2130 devices in the previous chapter. While different, since the change is small it is most likely due to fluctuations in the performance of the equipment used to fabricate 3-2130 versus IFA and IFB (the two groups were fabricated on separate days using shared equipment), considering surface resistivities over four orders of magnitude larger have been reported in MBE grown T2SL devices [42].

The second thing to note is that the bulk R_0A values for the IFB devices are actually lower than that of the IFA devices. This result was not expected considering the slightly higher light p-doping of IFB was expected to improve the electrical performance of the devices. One explanation could be that though the IFA devices have slightly better performance at zero bias, the electrical benefit actually occurs in the reverse bias regime, seen in Figure 5.2. As mentioned in the previous chapter, the maximum of the RA curve generally appears when the device is slightly reverse biased; this is why some state-of-the-art devices are operated in that regime instead of at zero bias. One other possibility is that the electrical benefit of the light p-doping does not follow a linear trend, though further investigation is required to prove or disprove this notion [41].

Though there are questions remaining about the electrical performance, the optical performance follows the expected trend. Though the benefit of light p-doping is better electrical performance due to the increase in the minority carrier electrons, a sacrifice is made in terms of the quantum efficiency and optical absorption, reducing their value (though not shifting the cutoff wavelength) [14]. Figure 5.5 plots the absolute responsivity of IFA (dashed) and IFB (solid) devices for three different sizes: 400 μm $\times$ 400 μm (a), 300 μm $\times$ 300 μm (b), and 200 μm $\times$ 200 μm (c). These curves were measured in an ABB Bomem DA-8 FTIR using a KBr beamsplitter and Globar source and calibrated using a spike filter at 4.845 μm. In each case the responsivity and specific detectivity of the higher p-doped IFB devices were less than that of the IFA devices, as predicted, and no change in cutoff wavelength was observed between the two different samples. However, despite operating at 4.5 K, the peak specific detectivities of these devices are more than an order of magnitude less than the specific detectivities of some state-of-the-art devices operating at 55 K [3].

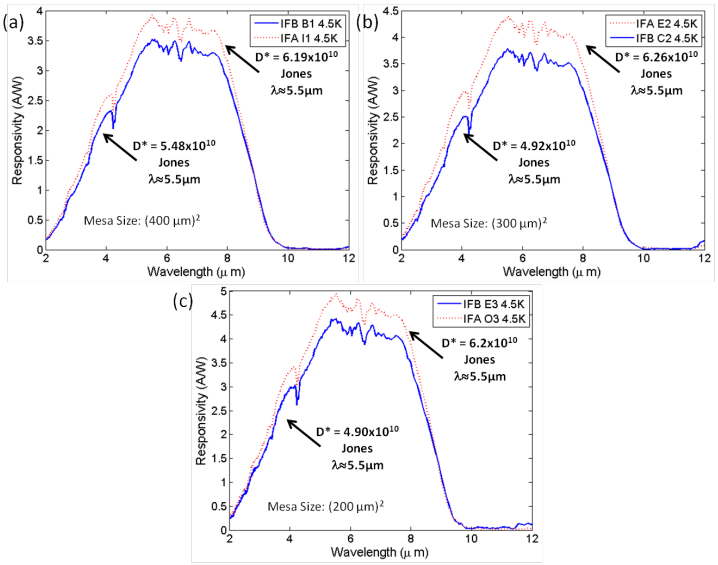

Figure 5.5: Comparison between the absolutely responsivity curves for IFA (dashed) and IFB (solid), taken at a temperature of 4.5 K. As expected, the increase in absorber region p-doping leads to a slight decrease in the responsivity of the IFB sample without changing the cutoff wavelength [14]. Devices of size 400 μm $\times$ 400 μm (a), 300 μm $\times$ 300 μm (b), and 200 μm $\times$ 200 μm (c) are shown.

CHAPTER 6

PASSIVATION OF T2SL PHOTODETECTORS

6.1 Surface Leakage Current

One of the most important dark current mechanisms that affects actual photodiode mesas is the surface leakage current that arises from the abrupt termination of the T2SL at the sidewall of a device, as well as the native oxides, such as In_2O_3, and residual materials formed on the sidewall surfaces during processing. The termination of the lattice at the sidewall results in dangling bonds located on the surface which bends the band in that region and pins the Fermi level above the conduction band. Native oxides formed due to exposure to the ambient environment of the sample during processing and byproducts of etching or mask materials can also facilitate the band bending if they are charged, or can act as trap states within the bandgap that increase the TAT current. The result is the formation of a depletion region under the surface, which must be eliminated to suppress the surface leakage current [43]. Some of the methods used to remove the dangling bonds or reduce the band bending at the interface are:

1. Soaking the sample in aqueous solutions of ammonium sulfide ($(NH_4)_2S$), which reduces the amount of surface oxides and produces passivating sulfide compounds [44].

2. Low-temperature deposition of a thin layer of SiO_2, which has also resulted in a decrease in dark current densities and increase in device resistances [20].

3. Encapsulation by electrically neutral polyimide [45], which, in one case, resulted in an R_0A product greater than 5300 Ωcm^2 when combined with an effective dry etching recipe and a wide bandgap barrier in the depletion region [42].

There are a few problems with using these passivation methods. Ammonium sulfide, though the most widely studied T2SL passivation scheme, has a very severe long-term degradation problem [43]. If the ammonium sulfide treated surface is exposed to high temperatures or even ambient atmosphere, the quality of the sulfur bonds that line the sidewall of the device will be compromised, and the device quality will actually drop to levels below its pre-passivation performance. One of the possible solutions for this problem is to encapsulate the device using polyimide immediately after soaking in ammonium sulfide. Thus, the device will retain the improved performance from the passivation soak, yet will be protected by the polyimide.

In recent years, more complex methods of passivation have been attempted. In 2005, a group from the Fraunhofer Institute in Germany reported the passivation of a 10 μm cutoff wavelength InAs/InGaSb T2SL using epitaxially overgrown $Al_{0.5}Ga_{0.5}As_{0.04}Sb_{0.96}$. This method is very difficult due to the need for the epitaxial layer to be lattice matched to the superlattice, though the results were extremely encouraging, producing devices with R_0A values of approximately 10 Ωcm^2 [46]. Also, just last year a group from Northwestern University used a gate controlled sidewall passivation scheme to nearly eliminate the surface leakage current in a 4.7 μm InAs/GaSb T2SL, leading to a specific detectivity of 2.5×10^{14} Jones, a 3.6 times improvement [47].

6.2 Passivation Using Ammonium Sulfide

This work focuses on the passivation of an MOCVD grown T2SL structure, 3-2155 ($\lambda_{cutoff} \cong 10.9$ μm), by a neutralized ammonium sulfide solution and a 4% ammonium sulfide solution. In this case, only the electrical properties were tested, with future work planned for optical characterization. The wafer consists of a highly n-doped (2×10^{18} cm^{-3}), 300 nm wide InAs buffer layer, grown on a nominally n-type (1×10^{16} cm^{-3}) InAs substrate. Next, the n-i-p superlattice is grown in the following order: 60 periods of graded n-doped (2×10^{18} cm^{-3} to 1×10^{16} cm^{-3}) InAs/GaSb (51.4 Å, 21.3 Å), followed by 200 periods of non-intentionally doped InAs/GaSb (51.4 Å, 21.3 Å), and 60 periods of graded p-doped (1×10^{16} cm^{-3} to 3.8×10^{18} cm^{-3}) InAs/GaSb (51.4 Å, 21.3 Å). The structure is capped by a highly p-doped (3.8×10^{18} cm^{-3}), 50 nm GaSb contact layer.

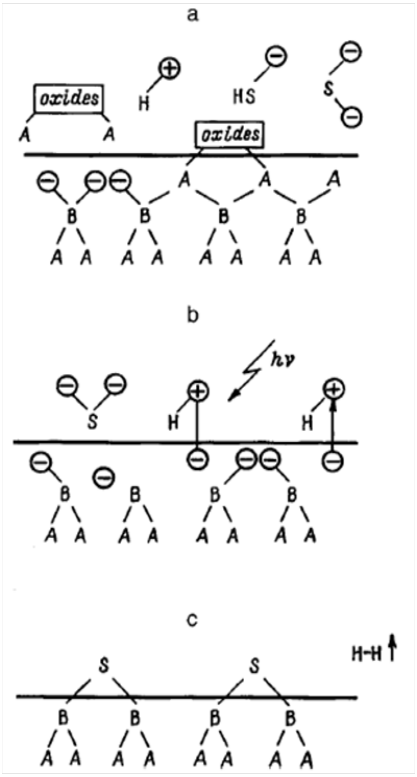

Figure 6.1: Diagram of the process by which ammonium sulfide (or any other chalcogenide) passivates the exposed sidewall of a III-V material, resulting in the removal of oxides and dangling bonds. From [48].

Figure 6.1 is a diagram of the process by which ammonium sulfide (or any other chalcogenide) operates on the sidewall of a III-V material (such as a T2SL). First, the bonds between the III and V atoms at the surface are broken, removing any oxides (a). Next, electrons are transferred into the solution from the semiconductor (b) and the sulfur atoms form bonds at the surface of the T2SL with different III-V atoms (c). This results in the formation of a passivating sulfur layer, which has removed any oxides or dangling bonds that would enable surface leakage dark currents.

Figure 6.2 is a set of current density vs. voltage (JV) plots for an ammonium sulfide solution neutralized by HCl to a pH of 7.0. First, the devices were fabricated using the dry etch process given in Chapter 3. After wire bonding, the unpassivated sample was tested at 78 K. Next, the sample was left to soak in the neutralized solution for one hour at room temperature, then dried with nitrogen and tested at 78 K within one hour of removal from the solution. It is immediately apparent from Figure 6.2 that there is a large

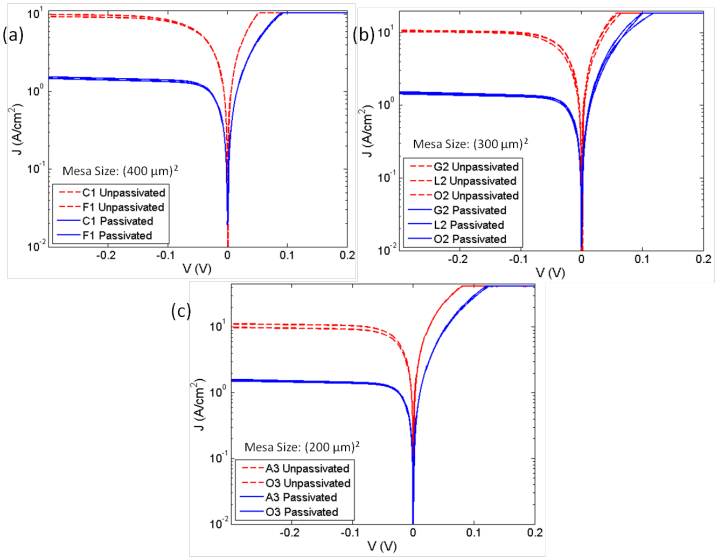

Figure 6.2: JV curves for before passivation (dashed) and after passivation (solid) with a neutralized ammonium sulfide solution for different sized devices, 400 μm $\times$ 400 μm (a), 300 μm $\times$ 300 μm (b), and 200 μm $\times$ 200 μm (c), at a temperature of 78 K. The neutralized ammonium sulfide solution results in a reduction in dark current of almost an order of magnitude for all device sizes.

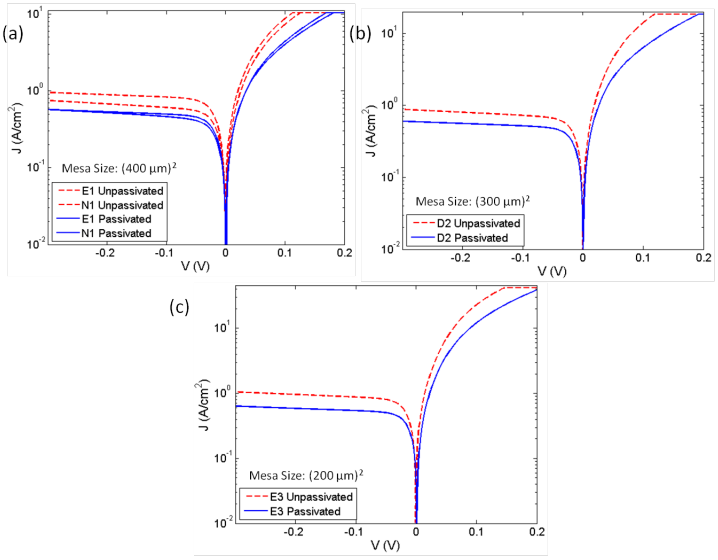

Figure 6.3: JV curves for before passivation (dashed) and after passivation (solid) with a 4% ammonium sulfide solution for different sized devices, 400 μm $\times$ 400 μm (a), 300 μm $\times$ 300 μm (b), and 200 μm $\times$ 200 μm (c), at a temperature of 78 K. The 4% ammonium sulfide solution results in a slight reduction of dark current, though the unpassivated performance was almost an order of magnitude better than the unpassivated performance of the devices in Figure 6.2, rendering direct comparisons useless.

Table 6.1: R_0A products before and after passivation using a neutralized ammonium sulfide solution.

Size (μm^2)	R_0A_{unpass} **(Ωcm^2)**	R_0A_{pass} **(Ωcm^2)**	**Increase**
(400 μm)^2	6.19×10^{-3}	1.90×10^{-2}	3.07
(300 μm)^2	4.22×10^{-3}	1.90×10^{-2}	4.50
(200 μm)^2	3.19×10^{-3}	1.48×10^{-2}	4.64

Table 6.2: R_0A products before and after passivation using a 4% ammonium sulfide solution.

Size (μm^2)	R_0A_{unpass} **(Ωcm^2)**	R_0A_{pass} **(Ωcm^2)**	**Increase**
(400 μm)^2	2.86×10^{-2}	4.98×10^{-2}	1.74
(300 μm)^2	2.74×10^{-2}	4.17×10^{-2}	1.52
(200 μm)^2	2.13×10^{-2}	3.66×10^{-2}	1.72

difference between the unpassivated (dashed) JV curves and the passivated (solid) curves. Though it is difficult to see, the unpassivated curves follow the same trend in the reverse bias as all the MOCVD and MBE devices mentioned in chapters 4 and 5, respectively. That is, as the device size decreases the dark current density increases due to the relationship between the surface leakage current and the P/A ratio.

However, after passivation the current density curves are exactly the same in the reverse bias, indicating the dark current has been greatly reduced. Not only that, each device size shows an almost order of magnitude reduction in dark current density. The increase in performance can also be seen in the R_0A product values, shown in Table 6.1, where the largest mesas show a 3.06 times increase in R_0A, the 300 μm $\times$ 300 μm mesas show a 4.5 times increase, and the 200 μm $\times$ 200 μm mesas show a 4.64 times increase.

A different ammonium sulfide solution is attempted on another sample of 3-2155, fabricated separately from the samples used for the neutralized solution. The results are shown in Figure 6.3 for different sized devices, 400 μm $\times$ 400 μm (a), 300 μm $\times$ 300 μm (b), and 200 μm $\times$ 200 μm (c), at a temperature of 78 K. In this case, the unpassivated devices (dashed) were tested immediately after fabrication and wire bonding at a temperature of 78 K. The sample was then left to soak for 30 minutes at room temperature in a 4% ammonium sulfide solution with a pH of 9.5. Once finished, the samples were dried with nitrogen and tested within one hour. Once again, the devices all show a reduction in dark current, though it is much smaller

than the devices tested with the neutralized solution. However, a fair comparison between the two different solutions cannot made due to the order of magnitude difference between their unpassivated dark current densities. Table 6.2 lists the unpassivated and passivated R_0A products, as well as the relative increase for each device size.

Despite the difference in unpassivated dark current density, it is clear that both solutions resulted in improved electrical performance of the 3-2155 devices. However, it is still undetermined which solution provides the larger amount. In order to have a fair comparison, the tested samples need to be fabricated simultaneously to ensure that the etching depth and processing conditions are exactly the same. Another problem has to do with the longevity of the passivation scheme. As mentioned previously, surface passivation using ammonium sulfide is actually very detrimental to the performance of the device if it is left exposed to the ambient atmosphere. Therefore, an effective passivation method would include an immediate polyimide spin and cure to encapsulate the device. The polyimide could then be etched off the tops and bottoms of the mesas, exposing them for contacts and optical measurements, leaving just the sidewalls covered. However, the initial improvement in the device performance is encouraging, despite the fact that even the passivated R_0A values are less than the unpassivated values for the 3-2130 devices presented in Chapter 4. This could be the result of any number of problems – design, growth, fabrication – but it is most likely the fact that the cutoff wavelength for 3-2155 is longer than for 3-2130 by over half a micron which, when in the LWIR, can cause a significant reduction in performance.

CHAPTER 7

CONCLUSION

7.1 Summary

In this work, InAs/GaSb type-II superlattices grown by both MOCVD and MBE were fabricated and tested. The relevant background information regarding infrared radiation and its applications was covered in Chapter 1, along with a brief description of two commercially available mid- to very long-wave infrared detectors, mercury cadmium telluride detectors and quantum well infrared photodetectors. The T2SL was then introduced and its method of operation, as well as its appeal with regards to MCT and QWIPs, was explained. Chapters 2 and 3 introduced the state-of-the-art for T2SLs, important figures of merit, novel structures, and the fabrication and characterization methods used to make and test T2SL devices. One of the key achievements of this work was the demonstration of the first generation of MOCVD grown T2SL devices on an InAs substrate. These devices were confirmed to have a 4.8 times increase in the R_0A product over the previous generation of MOCVD grown T2SLs (the first ever), which were grown on a GaSb substrate. Next, the effect of light p-doping in the absorber region was discussed and data was presented on two InAs/GaSb T2SLs grown via MBE. The two structures were identical except that the doping in the absorber region of sample IFB was slightly higher than that of IFA. The better electrical performance in the reverse bias by IFB was confirmed, though further testing is needed to determine the deviation from the trend at exactly zero bias. Also, the optical properties of the two samples were displayed, with IFA performing better than IFB by a slight margin (as expected), though both were over an order of magnitude behind the state-of-the-art T2SL devices at that cutoff wavelength. During the testing and analysis of both the MOCVD grown and MBE grown samples it was recognized that surface leakage cur-

rents were extremely prevalent, especially as the device size shrinks, and need to be eradicated if focal plane arrays for commercial use are to be fabricated or even if T2SL laboratory device performance is to approach that of its MCT counterpart. Therefore, a surface passivation scheme is necessary to reduce or eliminate the contribution to the dark current of this surface leakage. Two ammonium sulfide solutions, one that had been neutralized with HCl and the other with a 4% concentration of ammonium sulfide, were tested on devices fabricated from MOCVD grown T2SLs designed for a cutoff wavelength of approximately 11 μm. Both ammonium sulfide solutions improved the electrical performance of the devices, though the neutralized solution decreased the dark current by almost an order of magnitude, whereas the 4% solution was less effective. However, a comparison between the relative effectiveness of the two solutions could not be drawn because the initial, unpassivated performance of the devices that were tested differed by almost an order of magnitude, with the neutralized solution applied to the devices with larger dark currents. Therefore, more testing, preferably on devices fabricated simultaneously, is needed to fully compare the effectiveness of the different solutions.

7.2 Future Work

The growth of T2SLs via MOCVD, and the subsequent demonstration of their ability to operate as mid- to long-wave IR detectors, is the first step in an exciting new direction of T2SL photodetectors, one that could make them an enticing industry alternative to the current state-of-the-art MCT detectors due to the lower cost and higher throughput than even MBE grown T2SLs. The usage of an InAs substrate in place of a GaSb substrate also opens up many promising avenues of research, including the use of ternary compounds such as InAsSb with less-stringent requirements on strain management. However, in order for both the MOCVD and MBE grown devices to operate at state-of-the-art levels, it is clear that novel layer structures, such as those discussed in Chapter 2, will be needed due to their ability to reduce and suppress several dark current mechanisms if designed properly. Interfacial layer control will also play a large role T2SL performance improvement due to their large impact on the electrical properties of device level struc-

tures. Finally, an effective surface passivation scheme will be critical in not only increasing the initial performance of the device, but maintaining that performance level for significant periods of time. However, future passivation work on MOCVD T2SLs must be performed on devices with consistent unpassivated performance in order to draw fair comparisons between data sets. Since ammonium sulfide suffers severe degradation as both time and temperature increase, it is recommended that this passivation technique be combined with a physical encapsulation layer such as polyimide or SiN_x to preserve the stability of the sulfur bonds.

REFERENCES

[1] E. F. Schubert, "F18-02 Planck black body," 2004. [Online]. Available: http://www.ecse.rpi.edu/∼schubert/Light-Emitting-Diodes-dot-org/chap18/F18-02%20Planck%20black%20body.jpg

[2] S. L. Chuang, *Physics of Photonic Devices,* 2nd ed.. Hoboken, NJ: Wiley, 2009.

[3] G. J. Brown, "Type-II InAs/GaInSb superlattices for infrared detection: An overview," in *Infrared Technology and Applications XXXI*, Orlando, FL, USA, Mar. 2005, pp. 65–77.

[4] M. Z. Tidrow, "Type II strained layer superlattice: A potential future IR solution," *Infrared Physics & Technology*, vol. 52, no. 6, pp. 322–325, Nov. 2009.

[5] S. Krishnamurthy et al., "Tunneling in long-wavelength infrared HgCdTe photodiodes," *Journal of Electronic Materials*, vol. 35, no. 6, pp. 1399–1402, 2006.

[6] A. Gilmore et al., "Tunneling in long-wavelength infrared HgCdTe photodiodes," *Journal of Electronic Materials*, vol. 35, no. 6, pp. 1403–1410, 2006.

[7] L. Esaki and R. Tsu, "Superlattice and negative differential conductivity in semiconductors," *IBM Journal of Research and Development*, vol. 14, pp. 61–65, Jan. 1970.

[8] G. A. Sai-Halasz and L. Esaki, "InAs-GaSb superlattice energy structure and its semiconductor-semimetal transition," *Physical Review B*, vol. 18, no. 6, pp. 2812–2818, 1978.

[9] D. L. Smith and C. Mailhoit, "Proposal for strained type II superlattice infrared detectors," *Journal of Applied Physics*, vol. 62, no. 6, pp. 2545–2548, 1987.

[10] M. H. Young et al., "Recent advances in Ga1-xInxSb/InAs superlattice IR detector materials," *Applied Surface Science*, vol. 123-124, pp. 395–399, 1998.

[11] C. H. Grein et al., "Theoretical performance of very long wavelength InAs/In(x)Ga(1-x)Sb superlattice based infrared detectors," *Applied Physics Letters*, vol. 65, no. 20, pp. 2530–2532, Nov. 1994.

[12] C. H. Grein et al., "Minority carrier lifetimes in ideal InGaSb/InAs superlattices," *Applied Physics Letters*, vol. 61, no. 24, pp. 2905–2907, Dec. 1992.

[13] E. R. Youngdale et al., "Auger lifetime enhancement in InAs-Ga(1-x)In(x)Sb superlattices," *Applied Physics Letters*, vol. 64, no. 23, pp. 3160–3162, June 1994.

[14] P. F. Qiao et al., "Electronic band structures and optical properties of type-II superlattice photodetectors with interfacial effect," *Optics Express*, vol. 20, no. 2, pp. 2319–2334, Jan. 2012.

[15] Y. Huang et al., "InAs/GaSb type-II superlattice structures and photodiodes grown by metal-organic chemical vapor deposition," *Applied Physics Letters*, vol. 96, no. 25, p. 251107, Aug. 2010.

[16] A. Petschke et al., "Metal-organic chemical vapour deposition growth of InAs/GaSb type-II superlattice photodiodes," *Electronic Letters*, vol. 46, no. 16, pp. 1151–1152, Aug. 2010.

[17] D. Y. Zuo, "Antimonide-based type-II superlattice infrared photodetectors on indium-arsenide substrates," M.S. thesis, University of Illinois at Urbana-Champaign, Urbana, IL, 2011.

[18] J. D. Vincent, *Fundamentals of Infrared Detector Operation and Testing.* New York, NY: Wiley-Interscience, 1990.

[19] A. Rogalski, *Infrared Detectors,* 2nd ed.. Boca Raton, FL: CRC Press, 2011.

[20] A. Gin, "Passivation of type II InAs/GaSb superlattice photodiodes," *Thin Solid Films*, vol. 447-448, pp. 489–492, 2004.

[21] G. R. Belle and C. F. McConville, "Surface-plasmon modes in Zn-doped InAs(001) and (111)," *Physical Review B*, vol. 56, no. 24, pp. 15 995–16 002, Dec. 1997.

[22] L. O. Olsson et al., "Charge accumulation at InAs surfaces," *Physical Review Letters*, vol. 76, no. 19, pp. 3626–3629, May 1996.

[23] S. Mou et al., "Surface channel current in InAs/GaSb type-II superlattice photodiodes," *Journal of Applied Physics*, vol. 102, p. 066103, 2007.

[24] C. H. Grein et al., "Auger lifetimes in ideal InGaSb/InAs superlattices," *Journal of Electronic Materials*, vol. 22, no. 8, pp. 1093–1096, 1993.

[25] E. H. Steenbergen et al., "Significantly improved minority carrier lifetime observed in long-wavelength infrared III-V type-II superlattice comprised of InAs/InAsSb," *Applied Physics Letters*, vol. 99, p. 251110, 2011.

[26] Q. K. Yang et al., "Investigation of trap-assisted tunneling current in InAs/(GaIn)Sb superlattice long-wavelength photodiodes," *Applied Physics Letters*, vol. 81, no. 25, pp. 4757–4759, Dec. 2002.

[27] D. R. Rhiger, "Performance comparison of long-wavelength infrared type II superlattice devices with HgCdTe," *Journal of Electronic Materials*, vol. 40, no. 8, pp. 1815–1822, Apr. 2011.

[28] C. H. Grein et al., "Strained and unstrained layer superlattices for infrared detection," *Journal of Electronic Materials*, vol. 38, no. 8, pp. 1800–1804, Mar. 2009.

[29] B. Nguyen et al., "Very high quantum efficiency in type-II InAs/GaSb superlattice photodiode with cutoff of 12 μm," *Applied Physics Letters*, vol. 90, p. 231108, 2007.

[30] E. H. Aifer et al., "W-Structured type-II superlattice based long and very-long wavelength infrared photodiodes." in *Quantum Sensing and Nanophotonic Devices II*, Bellingham, WA, USA, 2005, pp. 259–272.

[31] E. H. Aifer et al., "W-Structured type-II superlattice long-wave infrared photodiodes with high quantum efficiency," *Applied Physics Letters*, vol. 89, p. 053519, 2006.

[32] I. Vurgaftman et al., "Graded band gap for dark-current suppression in long-wave infrared W-structured type-II superlattice photodiodes," *Applied Physics Letters*, vol. 89, p. 121114, 2006.

[33] B. Nguyen et al., "Type-II "M" structure photodiodes: An alternative material design for mid-wave to long wavelength infrared regimes," in *Quantum Sensing and Nanophotonic Devices IV*, 2007, p. 64790S.

[34] B. Nguyen et al., "Dark current suppression in type II InAs/GaSb superlattice long wavelength infrared photodiodes with M-structure barrier," *Applied Physics Letters*, vol. 91, p. 163511, 2007.

[35] D. Z. Ting et al., "A high-performance long wavelength superlattive complementary barrier infrared detector," *Applied Physics Letters*, vol. 95, p. 023508, 2009.

[36] E. K. Huang et al., "Inductively coupled plasma etching and processing techniques for type-II InAs/GaSb superlattices infrared detectors toward high fill factor focal plane arrays," in *Quantum Sensing and Nanophotonic Devices VI*, San Jose, CA, USA, 2009, pp. 72 220Z–8.

[37] S. Mou, "Theory and experiment of antimony-based type-II superlattice infrared photodetectors," Ph.D. dissertation, University of Illinois at Urbana-Champaign, Urbana, IL, 2007.

[38] P. R. Griffiths and J. A. D. Haseth, *Fourier Transform Infrared Spectrometry*. Hoboken, NJ: Wiley-Interscience, Mar. 2007.

[39] B. Nguyen et al., "Background limited long wavelength infrared type-II InAs/GaSb superlattice photodiodes operating at 110 K," *Applied Physics Letters*, vol. 93, p. 123502, 2008.

[40] A. Hood et al., "On the performance and surface passivation of type II InAs/GaSb superlattice photodiodes for the very-long-wavelength infrared," *Applied Physics Letters*, vol. 87, no. 15, pp. 151 113–3, 2005.

[41] S. Bandara et al., "Doping dependence of minority carrier lifetime in long-wave Sb-based type II superlattice infrared detector materials," *Optical Engineering*, vol. 50, no. 6, pp. 061 015–1, June 2011.

[42] E. K. Huang et al., "Surface leakage reduction in narrow band gap type-II antimonide-based superlattice photodiodes," *Applied Physics Letters*, vol. 94, pp. 053 506–1, 2009.

[43] J. Li, "Antimonide-based type-II quantum well infrared photodetectors," Ph.D. dissertation, University of Illinois at Urbana-Champaign, Urbana, IL, 2005.

[44] J. Li and S. L. Chuang, "Surface recombination velocity reduction in type-II InAs/GaSb superlattice photodiodes due to ammonium sulfide passivation," *Applied Physics Letters*, vol. 90, pp. 223 503–1, 2007.

[45] E. K. Huang et al., "Surface leakage reduction in narrow band gap type-II antimonide-based superlattice photodiodes," *Applied Physics Letters*, vol. 94, pp. 053 506–1, 2009.

[46] R. Rehm et al., "Passivation of InAs/(GaIn)Sb short-period superlattice photodiodes with 10 μm cutoff wavelength by epitaxial overgrowth with $Al_xGa_{1x}As_ySb_{1y}$," *Applied Physics Letters*, vol. 86, p. 173501, 2005.

[47] G. Chen et al., "Elimination of surface leakage in gate controlled type-II InA/GaSb mid-infrared photodetectors," *Applied Physics Letters*, vol. 99, p. 183503, 2011.

[48] V. Besselov and M. Lebdev, "Chalcogenide passivation of III-V semiconductor surfaces," *Semiconductors*, vol. 32, no. 11, pp. 1141–1156, Nov. 1998.